A&A 591, A105 (2016)
DOI: 10.1051/0004-6361/201527909


Astronomy & Astrophysics

# Physical properties of Galactic *Planck* cold cores revealed by the Hi-GAL survey⋆

S. Zahorecz[1,2], I. Jimenez-Serra[3,1], K. Wang[1], L. Testi[1], L. V. Tóth[2], and S. Molinari[4]

[1] European Southern Observatory, Karl-Schwarzschild-Str. 2, 85748 Garching bei München, Germany
e-mail: szahorec@eso.org
[2] Eötvös Loránd University, Department of Astronomy, Pázmány Péter sétány 1/A, 1117 Budapest, Hungary
[3] University College London, Department of Physics and Astronomy, Hampstead Road 132, NW1 2PS, London, UK
[4] INAF−Istituto Fisica Spazio Interplanetario, via Fosso del Cavaliere 100, 00133 Roma, Italy

Received 7 December 2015 / Accepted 10 March 2016

**ABSTRACT**

*Context.* Previous studies of the initial conditions of massive star and star cluster formation have mainly targeted infrared-dark clouds (or IRDCs) toward the inner Galaxy. This is because IRDCs were first detected in absorption against the bright mid-infrared (IR) background of the inner Galaxy, requiring a favorable location to be observed. By selection, IRDCs therefore represent only a fraction of the Galactic clouds capable of forming massive stars and star clusters. Owing their low dust temperatures, however, IRDCs are bright in the far-IR and millimeter and, thus, observations at these wavelengths have the potential to provide a complete sample of star-forming massive clouds across the Galaxy.

*Aims.* Our aim is to identify the clouds at the initial conditions of massive star and star cluster formation across the Galaxy and compare their physical properties as a function of Galactic longitude and Galactocentric distance.

*Methods.* We have examined the physical properties of a homogeneous Galactic cold core sample obtained with the *Planck* satellite across the Galactic plane. With the use of *Herschel* Hi-GAL observations, we characterized the internal structure of the most reliable Galactic cold clumps within the Early Cold Core (ECC) *Planck* catalog. By using background-subtracted *Herschel* images, we derived the $H_2$ column density and dust temperature maps for 48 *Planck* clumps covered by the *Herschel* Hi-GAL survey. We calculated and analyzed the basic physical parameters (size, mass, and average dust temperature) of these clumps as a function of location within the Galaxy. We also compared these properties with the empirical relation for massive star formation previously derived.

*Results.* Most of the *Planck* clumps contain signs of star formation. About 25% of the clumps are massive enough to form high-mass stars and star clusters since they exceed the empirical threshold for massive star formation. *Planck* clumps toward the Galactic center region show higher peak column densities and higher average dust temperatures than those of the clumps in the outer Galaxy. Although we only have seven clumps without associated YSOs, the Hi-GAL data show no apparent differences in the properties of *Planck* cold clumps with and without star formation.

**Key words.** ISM: clouds – stars: formation – infrared: ISM

## 1. Introduction

In contrast to low-mass stars, the process by which massive stars form remains poorly understood. The characterization of the initial conditions of massive star and star cluster formation is indeed challenging: massive stars are less common and have much shorter lifetimes than low-mass stars. The formation of massive stars and star clusters is believed to start in cold and dense molecular structures. When viewed against the bright Galactic mid-infrared (IR) background, these clouds are called infrared dark clouds (IRDCs). While some show evidence for ongoing star formation, others appear to be starless. Thus, IRDCs represent the best objects in which to study the initial conditions for massive star and star cluster formation. This has been verified by single-dish observations in low resolution (e.g., Pillai et al. 2006; Chambers et al. 2009) and interferometric observations in high resolution (e.g., Wang et al. 2011, 2012, 2014; Longmore et al. 2013; Tan et al. 2013; Zhang et al. 2015).

Some of the early studies of IRDCs focused on the characterization of the global physical properties of IRDCs using *Spitzer* 8 $\mu$m data, i.e., based on extinction maps (Rathborne et al. 2006, 2008; Peretto et al. 2010; Butler & Tan 2009). However, such studies have a statistical bias because IRDCs, by selection, only represent the population of dense clouds projected onto the bright background of the inner Galaxy, as they need a favorable location to absorb background infrared radiation. Not all the dark patches are real star-forming objects. IRDC catalogs based only on mid-infrared data indeed overestimate the number of real sources by a factor of ∼2 (Jackson et al. 2008). In addition, Wilcock et al. (2012) studied 3171 IRDC candidates within the $l$ = 300−330° region of the Hi-GAL survey. Only 38% of these candidates were bright at the Herschel wavelengths, and therefore associated with cold cloud structures. The other mid-infrared IRDC candidates are simply minima in the mid-infrared background.

An unbiased selection criterion to identify the whole Galactic population of massive prestar and precluster forming clouds is based on the emission properties of dust in the far-IR and submillimeter. The APEX Telescope Large Area Survey of the

⋆ *Herschel* is an ESA space observatory with science instruments provided by European-led Principal Investigator consortia and with important participation from NASA.

Galaxy (ATLASGAL; Schuller et al. 2009) and the CSO Bolocam Galactic Plane Survey (BGPS; Aguirre et al. 2011) have provided catalogs of submillimeter sources throughout the inner Galaxy. The outer Galaxy is however out of the coverage for these systematic surveys.

For the first time, the *Planck* satellite has provided an inventory of the cold condensations throughout the Galaxy. The *Planck* survey covered the submillimeter-to-millimeter wavelength range with unprecedented sensitivity, furnishing the first all sky catalog of cold objects. This is thus a perfect database to identify the coldest structures in the whole Galaxy, offering the opportunity to search for massive star-forming clumps in the outer Galaxy also and to investigate the dependence of massive star formation with location in the Galactic disk. While in extragalactic studies only the average star formation properties can be studied (Kennicutt & Evans 2012), a more detailed analysis can be performed in the Galaxy toward different environments (e.g., the Galactic center, spiral arms, and outer Galaxy). The angular resolution of the *Planck* observations is however scarce for a thorough study of these objects, and higher angular resolution observations are needed to obtain detailed information about the temperature, column density structure, and star formation content of these cold objects.

In this paper we present the analysis of the *Herschel* observations of 48 *Planck* sources that fall within the Hi-GAL (Molinari et al. 2010; Molinari 2011, 2012) survey area. We use the *Planck* ECC catalog, which provides continuum fluxes for over 900 *Planck* sources across a broad range of wavelengths (from 350 to 850 $\mu$m), to systematically analyze the distribution of cold clumps in the Galactic plane. The higher spatial resolution of *Herschel* PACS and SPIRE (Poglitsch et al. 2010; Griffin et al. 2010) makes it possible to examine the internal structure of these *Planck* sources and allows us to identify their high column density peaks and sample their deeply embedded sources with angular resolutions of $\sim$5″−36″. In Sect. 2 we present the sample and datasets used in this paper, including the distance estimate for our sample. In Sect. 3 we describe the analysis methods and results based on the Hi-GAL and *Planck* data. Finally, in Sect. 4 we discuss our results.

## 2. Data and sample selection

### 2.1. Planck catalogs of Galactic cold core objects

The *Planck* satellite (Tauber et al. 2010) has provided an all-sky submillimetre and millimetre survey covering the wavelengths around and longward of the intensity maximum of cold dust emission. While $\nu^2 B_\nu(T = 10\ \mathrm{K})$ peaks close to 300 $\mu$m, the coldest dust with a temperature of $T \sim 6$ K shows its maximum emission close to 500 $\mu$m. Combined with far-infrared data such as the IRAS survey, the data enable accurate determination of both the dust temperature and spectral index. The Early Cold Cores[1] Catalogue (ECC; Planck Collaboration XXIII 2011) is part of the *Planck* Early Release Compact Source Catalogue (ERCSC) and the ECC forms a subset of the full Cold Core Catalogue of *Planck* Objects (C3PO; more than 10 000 objects have been detected; Planck Collaboration XXIII 2011). The ECC, with a total of 915 objects over the sky, contains only the most secure detections (signal-to-noise ratio $(S/N) > 15$) with color temperatures below 14 K.

[1] These "cores" are loosely defined as compact sources seen by the *Planck*, thus *Planck* "cores" have a wide range of physical sizes depending on distances. They are different than the 0.1 pc "cores" usually adopted by the star formation community.

The *Planck* Catalogue of Galactic Cold Clumps (PGCC; Planck Collaboration 2015) is the last release of *Planck* clump data tables. It contains 13188 Galactic sources with a temperature ranging from 5.8 K to 20 K. Forty-two percent of these sources have available distance estimates. A few ECC sources are not part of the PGCC catalog because they do not satisfy the compactness criterion of the PGCC catalog, i.e., they are slightly more extended compared to the other sources. We note however that the old ECC and new PGCC data are in good agreement for the selected 48 clumps. Indeed, the derived dust temperatures, spectral indices, and clump sizes differ by less than 6%, 1.5%, and 2%, respectively.

### 2.2. Planck ECC sources in the Hi-GAL survey

We selected the ECC sources that were also covered by the Hi-GAL survey to build up our sample. Hi-GAL was one of the Herschel Open Time Key Projects (Molinari et al. 2010) and, with its extensions (in OT1 and Hi-GAL2pi; Molinari 2012, 2011), this survey mapped the entire Galactic Plane of the Milky Way ($-1° < b < +1°$, following the Galactic warp) in five bands with the PACS instrument at 70 and 160 $\mu$m and with the SPIRE instrument at 250, 350, and 500 $\mu$m with spatial resolutions of 5″, 13″, 18″, 25″ and 36″, respectively.

We selected the 48 ECC sources that were also covered by the Hi-GAL survey (see Table A.1). These are all the ECC objects that fall within the *Herschel* Hi-GAL survey area and all five *Herschel* band images are available for each source. Three sources from our sample are not part of the latest PGCC catalog owing to their lower level of compactness (G001.64-00.07, G201.13+00.31, and G296.52-01.19), but we included these sources in our analysis. Based on their physical properties, there are no significant differences between these three rejected ECC clumps and the rest of the ECCs within the Hi-GAL region (see later in Sect. 3.3).

The main parameters associated with the *Planck* clumps are shown in Table A.1. The mass calculation based on *Planck* data is described in Sect. 3.1.

### 2.3. Distance determination of ECC objects

Distance determination is needed for the mass and size calculation of the ECC clumps. For this purpose, association with known IRDCs and molecular line follow up survey data were used. Table B.1 shows all the available estimated distances for the ECC objects and the final adopted distances. The data come from different sources:

1. Kinematic distance based on the CO $J = 1-0$ survey data of the Purple Mountain Observatory by Wu et al. (2012). CO $J = 1-0$ emission is detected in all ECC clumps except one. Among these sources, 28 clumps belong to our Hi-GAL ECC sample and have velocity and distance estimates in the Wu et al. (2012) survey. Half of them (15 sources) show more than one velocity components. In those cases, we used the velocity component with the brightest line intensity to estimate the distance of the ECC clump.
2. Kinematic distance based on the MALT90 (Millimetre Astronomy Legacy Team 90 GHz, ATNF Mopra 22-m telescope; Jackson et al. 2013) survey data. Six ECC clumps were covered by this survey. For the clumps with more than one molecular line detected (i.e., $N_2H^+$, $^{13}CO$, and $^{12}CO$), we adopted the kinematic distance derived from the species with higher critical density.

3. Kinematic distance based on our own APEX observations (Zahorecz et al., in prep.). APEX observations were performed toward three ECC clumps as part of the E-093.C-0866A-2014 project. Again, the kinematic distance adopted for these clumps was that associated with the emission from the species with higher critical density.
4. Kinematic distance based on the CfA CO survey (Dame et al. 2001) data. Twenty-four objects out of our sample of 48 *Planck* clumps show a single or dominating velocity component in the CfA $^{12}$CO survey data. In Fig. 1, we show some examples of the CfA CO survey spectra measured for the ECC sources that do not have any distance estimate from the Purple Mountain Observatory survey.
5. Associations with known IRDCs. Six ECC clumps are associated with known IRDC objects. Their kinematic distances were obtained by Parsons et al. (2009) based on the Galactic Ring Survey data.
6. Distance from the *Planck* PGCC catalog. This distance determination available in the PGCC catalog was obtained using several methods: kinematic distance estimates, optical extinction based on SDSS DR7, near-IR extinction toward IRDCs, and near-IR extinction. In case of the near-IR extinction methods, negative values indicated upper limits.

The distance flags for the ECC clumps considered in our sample are indicated in Table A.1. Once the molecular line velocity information was collected for our sample, we estimated the kinematic distance of the ECC clumps using the rotation curve of the Galaxy from Reid et al. (2014). We employed the publicly available Fortran code from Reid et al. (2009) to relate the radial velocity to the source's Galactrocentric radius. In the inner Galaxy, this Galactocentric radius corresponds to two distances along the line of sight: the near and far kinematic distances. The near kinematic distance was adopted if kinematic distance estimation alone was available for the source. For the sources in the outer Galaxy, the distance solution is unique.

We note that in 12 cases, both kinematic- and extinction-based distance estimates are available. The average difference between these two methods is 10%, although for two objects they differ by more than 50%. When an extinction-based distance estimate was available, we used that as the adopted distance (see Table A.1) since this method reproduces maser parallax distances (with very low level of uncertainties) better than kinematics distances (see Foster et al. 2012). Otherwise, we adopted the kinematic distance estimates obtained for the remaining ECC clumps.

Calculations of mass, size, and $H_2$ column density were performed only for the 40 clumps with available distance estimations. The distances are between 0.1 kpc and 8.1 kpc, the angular sizes lie between $4'-15'$, which give us spatial scales in the range of 0.5 pc−29 pc.

We note that the distance estimates for the majority (92%) of our ECC clumps are likely correct within a factor of 2, and so our mass estimates also lie within a factor of 4. Only three sources (i.e. 8% of the sample) may have distance discrepancies as large as a factor of 5, implying a factor of 25 uncertainty in the calculated mass. Therefore, our results on the mass distribution of ECC clumps as a function of Galactic longitude and Galactocentric distance are not expected to change substantially because the errors in the distance determination.

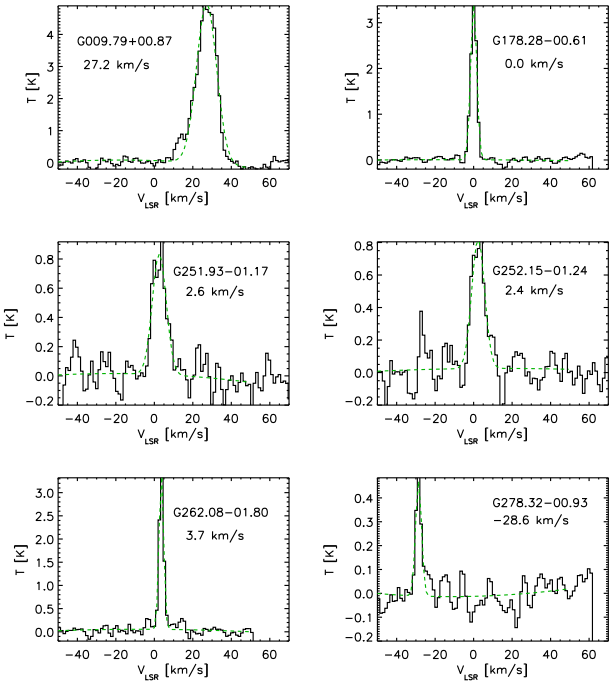


**Fig. 1.** Sample of CfA spectra toward the ECC clumps outside the Wu et al. (2012) survey. Green line shows the fitted Gaussian component centered at the velocity shown in the *top left panel.*

### 2.4. Location within the Galaxy

Once the distance of the selected ECC clumps has been estimated, we can determine the location where these objects fall within the Galaxy. Figure 2 shows the Galactic distribution of the selected clumps. The figure shows that 1/3 and 2/3 of these clumps are located in the inner and outer part of the Galaxy, respectively, between Galactic longitudes of 278° to 89° and 144° to 262°. Based on our estimated distances, 60% of these clumps fall on top of the Galactic spiral arms as defined in Reid et al. (2014).

## 3. Methods and results

### 3.1. Mass determination based on Planck data

From the fluxes measured by *Planck* for every cold clump and provided in the ECC catalog, we can estimate their individual masses using

$$M = \frac{S_\nu D^2}{\kappa_\nu B_\nu(T)}, \quad (1)$$

where $S_\nu$ is the integrated flux density, $D$ is the distance, $\kappa_\nu$ is the dust opacity, and $B_\nu(T)$ is the *Planck* function for dust temperature at $T$. The dust opacity was adopted by Planck Collaboration XXIII (2011) as

$$\kappa_\nu = 0.1 \times \left(\frac{\nu}{1\ \mathrm{THz}}\right)^\beta\ \mathrm{cm}^2/\mathrm{g}. \quad (2)$$

For this calculation, we used the integrated flux density at the frequency $\nu = 857$ GHz from the ECC catalog, the derived core temperature, $T_{\mathrm{core}}$, and the emissivity spectral index, $\beta_{\mathrm{core}}$. We note that the *Planck* fluxes at $\nu = 857$ GHz were used for the computation because this frequency is the closest one to the frequency reference (i.e., 1 THz) for the formula of the dust opacity (see Eq. (2)), so that the impact on the spectral index $\beta$ remains small compared to the uncertainty in $\kappa_\nu$. In addition, the

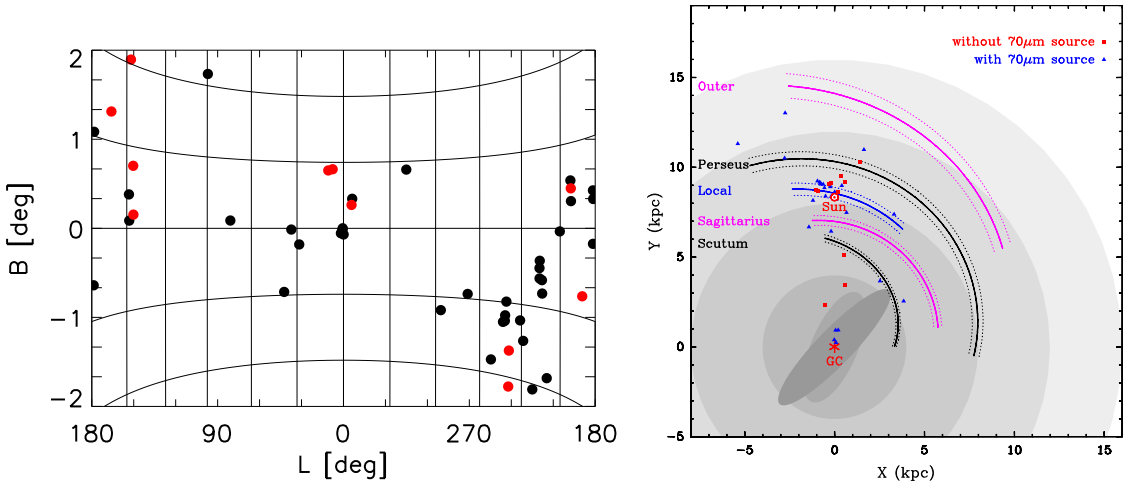


**Fig. 2.** *Left*: Galactic distribution of the selected 48 ECC clumps observed by the Hi-GAL project in Galactic latitude and longitude. *Right*: plan view of the Milky Way (Reid et al. 2014) with the 40 ECC clumps with available distance estimates overplotted. Red and blue symbols indicate the clumps from Category I and II, respectively (see Sect. 3.2 for the definition of these two categories). The position and $1\sigma$ width of spiral arms (Reid et al. 2014) are indicated with solid and dotted lines, respectively. The background gray disks with radii of ∼4 kpc, ∼8 kpc, ∼12 kpc, and ∼16 kpc indicate the Galactic bar, solar circle, co-rotation of the spiral pattern, and end of major star formation regions, respectively.

857 GHz band also has the best S/N of all *Planck* observations and dust emission at this frequency is optically thin (see details in Planck Collaboration XXIII 2011).

The average calculated mass based on the *Planck* data is $1.2 \times 10^6$ $M_\odot$ with a minimum and maximum value of 10 $M_\odot$ for G089.62+02.16 and $2.7 \times 10^7$ $M_\odot$ for G000.65-00.01, respectively. This average value is biased by a few very massive sources within the sample. The 25th, 50th, and 75th percentile of the data are $1.6 \times 10^2$ $M_\odot$, $1.7 \times 10^3$ $M_\odot$, and $2.2 \times 10^4$ $M_\odot$, respectively.

### 3.2. Clump categories based on Hi-Gal 70 μm data

In this section, we evaluate the level of star and star cluster formation within the *Planck* cold clumps observed by *Herschel* with the 70 $\mu$m Hi-GAL images. We note that the 70 $\mu$m images have the best angular resolution within the Hi-GAL data and therefore provide information about the point-like sources found within the clumps and likely associated with protostellar objects. Also it is an excellent probe of the population of intermediate- and high-mass young stellar objects in star-forming regions (see, e.g., Ragan et al. 2012; Veneziani et al. 2013). *Planck* clumps without 70 $\mu$m sources are the best candidates to study the earliest phases of star formation, since the absence of 70 $\mu$m emission likely indicates that protostellar activity has affected its surrounding environment very little.

In order to investigate whether there are significant differences in the physical properties (i.e., dust temperature, mass, and maximum $H_2$ column density) between clumps with and without star formation, we divided the sample of *Planck* cold clumps into two different categories: clumps with no sign of star formation (Category I, 11 sources) and clumps with active star formation (Category II, 37 sources).

We probe the star formation activity by checking the presence or absence of 70 $\mu$m point sources within the defined clump boundaries (see Sect. 3.3). From our classification of clumps with or without 70 $\mu$m point-sources, we find that 11 clumps (23% of the sample of 48 clumps) do not show any star formation activity. The criterion may be distant dependent because of the sensitivity of the 70 $\mu$m observations. To check for this possible bias, we plotted the distribution of ECC clumps with and without 70 $\mu$m sources as a function of distance (see Fig. 3). We find that sources without 70 $\mu$m sources are not, on average, further away than sources with 70 $\mu$m emission. On the contrary, most of the cores with no 70 $\mu$m sources lie within ∼4.5 kpc from the Sun with only one exception, i.e., G354.81+00.35 at ∼6 kpc.

Figure 4 shows examples of Category I (G146.71+2.05) and Category II (G319.35+0.87) clumps. *Herschel* 70, 250, and 500 $\mu$m images are shown with angular resolution of 5″, 18″, and 36″, respectively. A similar set of figures is available for all the 48 sources in Appendix A.

To investigate the possibility of chance alignments, we estimated the expected number of point sources within the clump regions. For this, we identified the sources present within 2 × 2 sq. deg Hi-GAL 70 $\mu$m tiles using SExtractor (Bertin & Arnouts 1996). Except for the ECC clumps located in the inner 20 deg of the Galaxy, the expected number of point sources due to chance alignment is less than 2 (median values of 0.02 for $|l-180°| < 90°$ and of 1.8 for $90° < |l - 180°| < 170°$), which implies that the 70 $\mu$m sources detected in the ECC clumps genuinely trace the star formation activity within the clumps. For the ECC clumps in the Galactic center, we note however that the number of expected sources by chance alignment is higher than for the ECC clumps in the Galactic disk (median value of 78 for $|l - 180°| > 170°$). This is related to the $H_2$ column density value chosen to define the clump boundary ($3 \times 10^{21}$ cm$^{-2}$, see Sect. 3.3), which covers larger areas. In any case, even for these Galactic center ECC clumps, the number of 70 $\mu$m sources detected in the Hi-GAL images is, on average, higher than the expected number of sources by chance alignment.

From the integrated flux of the faintest detected 70 $\mu$m point sources, we can estimate the luminosity (and mass) limit below which no source is detected in the Hi-GAL images. The faintest detected sources in the ECC clumps have fluxes $F_{70} \sim 45$ mJy. In order to make the conversion from 70 $\mu$m flux to luminosity, we use the following correlation (see Dunham et al. 2008):

$$L_{\rm int} = 3.3 \times 10^8 F_{70}^{0.94} \left(\frac{d}{0.14\ \rm kpc}\right)^2 L_\odot, \quad (3)$$

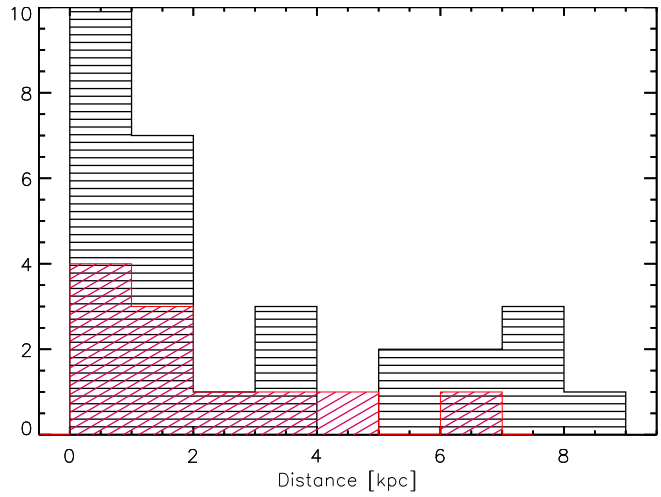


**Fig. 3.** Distribution of the ECC clumps as a function of distance. Red and black histograms indicate the clumps from Category I (clumps without 70 $\mu$m sources) and Category II (clumps with 70 $\mu$m sources), respectively.

where $F_{70}$ is in [ergs cm$^{-2}$ s$^{-1}$] and is normalized to 0.14 kpc and $d$ is the distance in kpc. The faintest sources in our ECC clumps (with $F_{70}$ = 45 mJy) have luminosities 0.2 – 0.7 – 1.5 – 2.6 $L_{\odot}$ at 1 – 2 – 3 – 4 kpc. For distances larger than 3 kpc, only high-mass protostars are luminous enough to be visible.

The all-sky YSO candidate catalogs of Tóth et al. (2014) and Marton et al. (2016) can be used to search for low- and intermediate-mass star formation. We find that four of our ECC clumps without 70 $\mu$m point sources show AKARI or WISE YSOs. This implies that, although these clumps have not formed massive protostars yet, they show a certain level of low-mass star formation. From this, the total number of clumps without any star formation activity (low mass and high mass) within their clump boundaries is reduced to seven, which represents 15% of the whole sample. Since we are mostly interested in the potential of the ECC clumps to form massive protostars, we hereafter focus on clump classification based on the presence or absence of 70 $\mu$m sources alone.

### 3.3. Physical properties derived from Hi-GAL data

The higher angular resolution of the *Herschel* Hi-GAL observations allows us to investigate not only the internal physical structure (compactness and fragmentation) of the *Planck* cold clumps, but also the small-scale variations in the dust temperature and $H_2$ column density distribution of these clumps. These higher angular resolution data also provide more accurate estimates of the fraction of the mass locked into the densest parts of the clumps, i.e., into the regions that form massive stars and star clusters.

Dust temperature ($T_{\rm dust}$) and $H_2$ column density maps ($N(H_2)$) were derived by fitting the SED constructed based on the *Herschel* PACS 160 $\mu$m and SPIRE 250−500 $\mu$m data pixel by pixel (see the detailed description of the method in Wang et al. 2015). As a first step, we smoothed the maps to the SPIRE 500 $\mu$m data resolution (i.e., to 36″) and we performed background subtraction. See Appendix C for a detailed description of the background subtraction methods we tested. As an example, Fig. 5 shows the 70 $\mu$m images (left) and calculated column density (middle) and dust temperature (right) maps for ECC G146.71+02.05 and G319.35+0.87.

To derive the mass, average temperature, and size of the clumps, we defined the boundaries of the clumps on the background-subtracted $H_2$ column density maps. The peak column density values span 2 order of magnitudes, so we used two different column density thresholds for the source definition: $3\times10^{21}$ cm$^{-2}$ and $10^{22}$ cm$^{-2}$. These values correspond to extinctions of ∼3 mag and ∼9 mag, respectively (see Güver & Özel 2009). These thresholds are shown in Fig. 5 in red (for $N(H_2)$ = $10^{22}$ cm$^{-2}$) and yellow contours (for $N(H_2)$ = 3 × $10^{21}$ cm$^{-2}$). The different column density thresholds give us information about the fraction of mass associated with the diffuse structure of the clump and the densest parts of the clumps, where star formation is expected to occur.

We note that for one clump, G249.23-01.64, the derived peak column density is smaller than 3 × $10^{21}$ cm$^{-2}$, and therefore its average dust temperature, mass, and size, within the $3\times10^{21}$ cm$^{-2}$ and $10^{22}$ cm$^{-2}$ contours, could not be calculated (see Table A.1). We do not detect 70 $\mu$m sources in G249.23-01.64. The peak column density is smaller than $10^{22}$ cm$^{-2}$ for 24 clumps; for 12 of these clumps we have multiple subclumps. In this case, the total mass of the clump was calculated as the addition of the subclump masses. For four sources in the Galactic centre region, the peak column density is larger than $10^{22}$ cm$^{-2}$, but the masses, sizes, and temperatures within the contours we used were not calculated because the size within these column density limits is not comparable with the size of the ECC. The region within the column density limit of 5−10 × $10^{22}$ cm$^{-2}$ is comparable with the size of the ECC objects.

In order to provide a characteristic dust temperature for the ECC clumps based on the Hi-GAL data, a column density weighted temperature was calculated within the clump boundary for every object. In this way, the derived temperature is dominated by the temperature of the dense material. The average temperature among all ECC clumps is 13.9 K based on the *Herschel* images, while the average dust temperature based on the *Planck* data differs by 1.5−3.0 K with respect to the *Herschel* one. This difference is discussed in more detail in the next section.

In Table A.1, we report all the calculated average temperatures, sizes, and masses values based on the two column density limits of $10^{22}$ cm$^{-2}$ and $3\times10^{21}$ cm$^{-2}$.

### 3.4. Distribution of the ECC physical properties with Galactic longitude and Galactocentric distance

After calculating the average $H_2$ column densities, dust temperatures, and masses of the ECC clumps from the *Herschel* data, we can investigate whether variations in these properties are observed depending on the location of the ECC clumps within the Galaxy.

In Fig. 6, we show the maximum $H_2$ column density distribution of the ECC clumps as a function of Galactic longitude and Galactocentric distance. ECC clumps toward the Galactic center region show the highest peak column density values. The peak column density decreases with Galactocentric distance. There is a 3 order of magnitude difference between the peak $N(H_2)$ values in the Galactic center region and in the outer part of the Galaxy. From Fig. 6, we also find that $H_2$ peak column densities $N(H_2) > 9\times10^{23}$ cm$^{-2}$ are only detected toward the Central Molecular Zone region. No high column density clumps with $N(H_2) > 10^{23}$ cm$^{-2}$ are found in the outer Galaxy. There is no clear trend between Category I and Category II clumps and their location within the Galaxy. These two types of clumps are found indistinctly across the Galaxy.

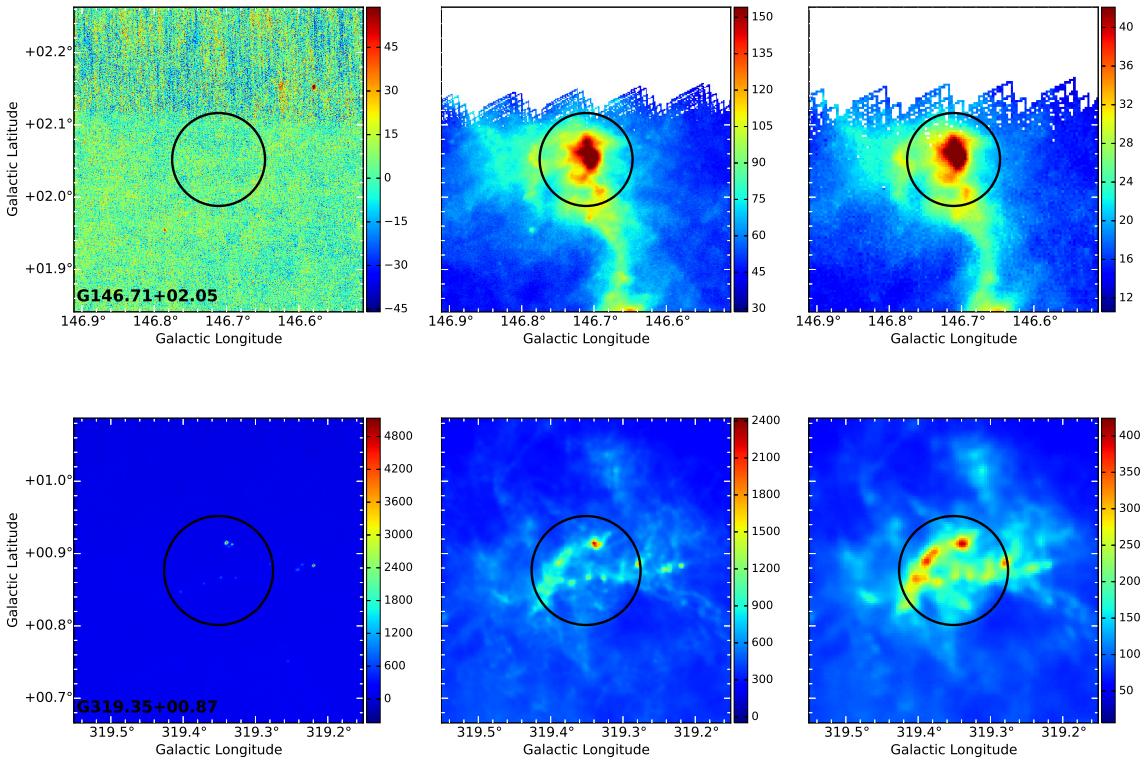


**Fig. 4.** *Herschel* 70, 250, and 500 $\mu$m images in MJy/sr of G146.71+2.05 and G319.35+0.87 from Category I and II, respectively, with a resolution of 5″, 18″, and 36″. Black circle shows the position of the *Planck* clump and major axis as shown in the ECC catalog.

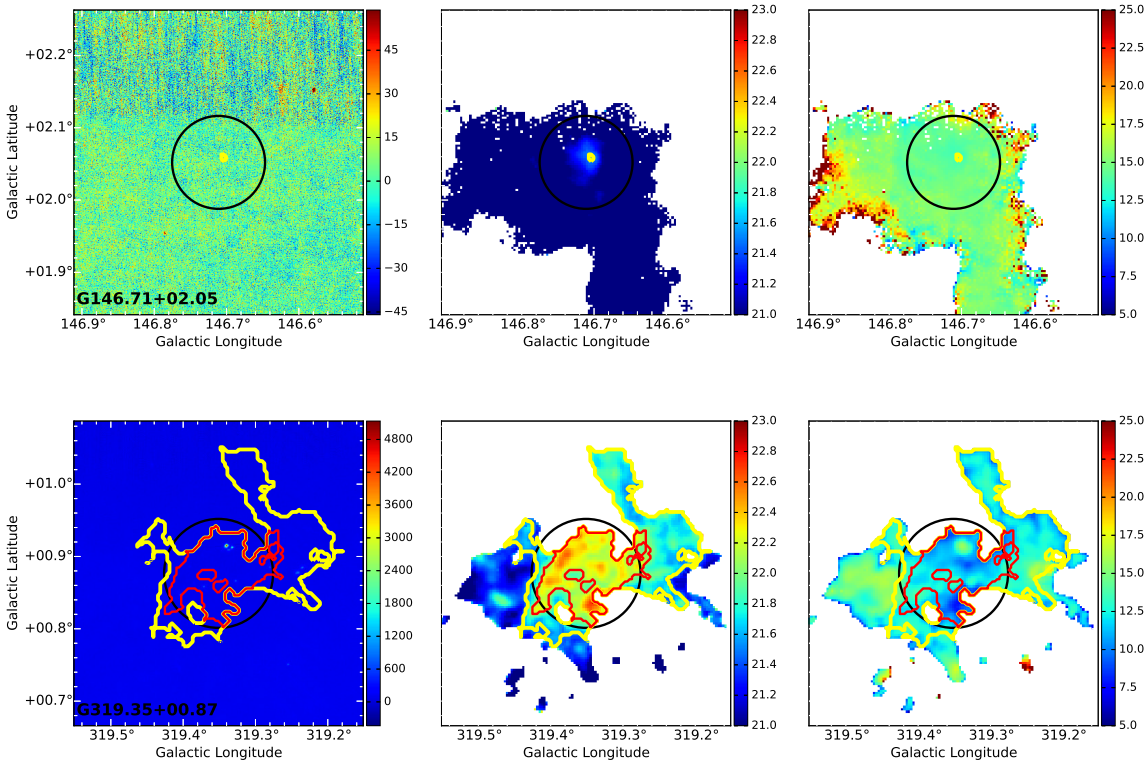


**Fig. 5.** 70 $\mu$m images ([MJy/sr], *left*) and calculated column density ([cm$^{-2}$], *middle*) in logarithmic scale and dust temperature ([K], *right*) maps for the same clumps shown in Fig. 4, ECC G146.71+02.05 (*top*) and G319.35+0.87 (*bottom*), from Category I and II with a resolution of 36″. Yellow and red contour levels refer to the $H_2$ column density thresholds $3 \times 10^{21}$ and $10^{22}$ cm$^{-2}$, respectively. Black circles are centered at the position of the *Planck* clump and circle sizes correspond to the major axis given in the ECC catalog.

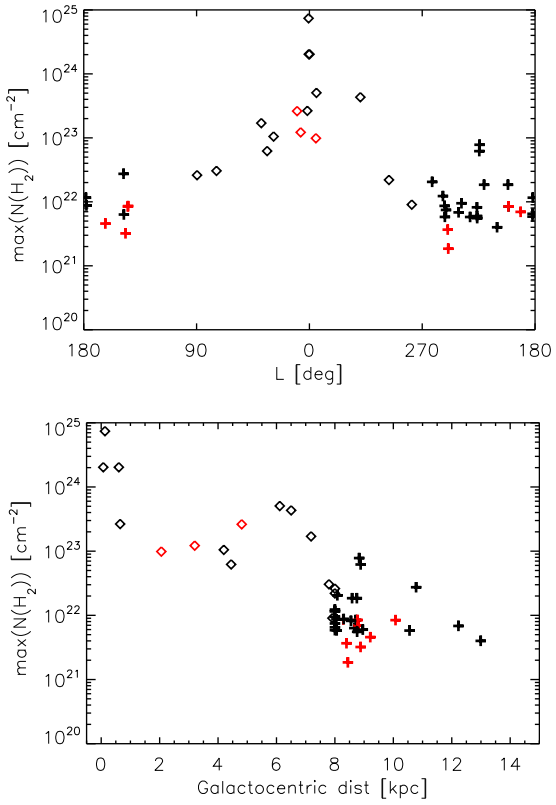


**Fig. 6.** Peak $H_2$ column density distribution of the ECC clumps as a function of Galatic longitude for the 48 objects (*top*) and Galactocentric distance for the 40 clumps with available distance estimates (*bottom*). Red symbols indicate the clumps without 70 $\mu$m point sources.

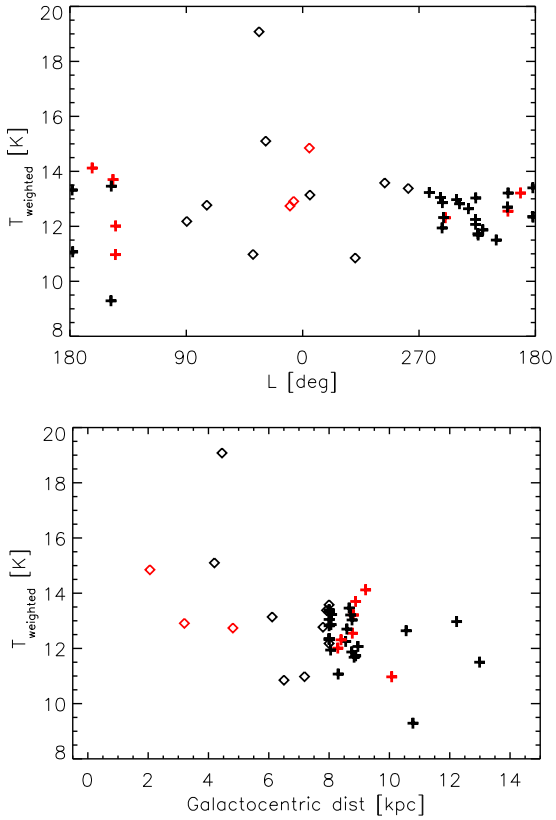


**Fig. 7.** Column density weighted average temperature distribution of the ECC clumps as a function of Galactic longitude for the 43 objects (*top*, four sources in the Galactic center region and a low column density source are excluded; see details in Sect. 3.3) and as a function of Galactocentric distance for the 35 clumps with available distance and average temperature estimates (*bottom*). Red symbols indicate the clumps without 70 $\mu$m point sources.

Figure 7 shows the column density weighted temperature, $T_{\rm weighted}$, distribution of the ECC clumps as a function of Galactic longitude and Galactocentric distance. Figure 7 also shows similar trends as the distribution of the maximum column density values. ECC objects in the Galactic center show higher temperatures (by more than 5 K difference). For the clumps with Galactocentric distances larger than 6 kpc, there is no significant difference in the calculated temperature between clumps with (in red) and without (in black) 70 $\mu$m sources. For Galactocentric distances shorter than 6 kpc, we have too few sources to draw conclusions. The weighted temperature outside the molecular ring is ~13 K, and values larger than 14.5 K are only detected within the molecular ring.

### 3.5. Comparison of Planck and Hi-GAL temperatures

In Fig. 8, we make the comparison between the clump dust temperature calculated from *Planck* data, $T_{\rm ECC}$, and the column density weighted average dust temperature derived from the *Herschel* images, $T_{\rm weighted}$. The *Planck* and *Herschel* based temperatures agree within ±3 K, except for the warmer sources in the Galactic center region, where our column density criteria select a much larger region than the *Planck* clump size and includes warmer regions. The average temperatures in the inner Galaxy are 10.4 K and 15.4 K based on the *Planck* and *Herschel* data, respectively. The same values are 11.8 K and 12.5 K in the outer part of our Galaxy. We note that there is one outlier clump in the outer Galaxy without any 70 $\mu$m emission (G201.26+00.46), for which the *Planck* based temperature is higher by ~5 K with respect to the average temperature derived from *Herschel* data. A bright 70 $\mu$m-emission region with high dust temperatures is visible toward the southwest from the clump. The *Planck* ECC size is larger than the denser region used in the *Herschel*-based calculation, which causes lower weighted temperature for the *Herschel* data. This comparison shows that the *Planck* ECC temperatures are, in most cases, a reasonable approximation for the average temperatures of the high column density regions of the cores. Temperatures derived from the integrated *Herschel* fluxes within the two column density contours that we used in the paper lead to the same conclusion.

## 4. Discussion

In this section, we evaluate the potential of forming massive stars and star clusters by the selected *Planck* cold clumps and determine their evolutionary stage. We accomplished this using the column density maps and bolometric luminosities based on the *Herschel* observations. In Sect. 4.1 we investigate the fraction of mass in the densest parts of the clumps compared to their surrounding, more diffuse regions, while in Sect. 4.2 we identify the clumps with ongoing massive star formation as probed by 70 $\mu$m emission. Kauffmann & Pillai (2010) showed that regions forming massive stars are, at a given radius, more massive than the limit mass ($m_{\rm lim}[r]$ = 870 $M_\odot[r/{\rm pc}]^{1.33}$) and thus, we evaluate the fraction of *Planck* cold clumps with the potential to form massive stars and star clusters.

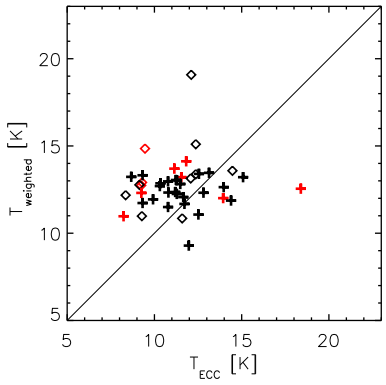


**Fig. 8.** $T_{\rm ECC}$ vs. $T_{\rm weighted}$ distribution. Red symbols indicate the clumps without 70 $\mu$m point sources. Plus signs indicate the clumps in the outer part of the Galaxy and diamonds indicate the sources in the inner Galaxy.

### 4.1. Mass distribution

As mentioned in Sect. 3.3, the clump masses and sizes were calculated from the Hi-GAL column density maps considering two different $H_2$ column density thresholds of $3 \times 10^{21}$ and $10^{22}$ cm$^{-2}$. The comparison of the masses contained within these levels gives us information about the fraction of gas mass locked into the densest parts of the clumps and the total mass enclosed within the surrounding region. This parameter may be important since it is possible to increase the total mass of the dense core through the accretion of this lower column density material.

Figure 9 shows the mass distribution of the sources as a function of Galactocentric distance. The top panel shows the total mass associated with a column density limit of $3 \times 10^{21}$ cm$^{-2}$, while the bottom panel shows the mass contained within the high column density gas, $N(H_2) > 10^{22}$ cm$^{-2}$. Solid lines show the range of masses and Galactocentric distances for the sources with large distance discrepancies. No sources with mass above $10^4$ $M_\odot$ were detected at a Galactocentric distance larger than 6 kpc. All the densest clumps with $N(H_2) > 10^{22}$ cm$^{-2}$ are found within 9 kpc to the Galactic center.

Figure 10 shows the size and mass ratio for the two column density thresholds considered, $3 \times 10^{21}$ cm$^{-2}$ and $10^{22}$ cm$^{-2}$, and the mass ratio as a function of Galactocentric distance. The ECC clumps with a Galactocentric distance of >9 kpc do not have high column density gas in our sample. The fraction of the mass in the densest parts of the nearby *Planck* clumps is lower than that of the more massive clumps closer to the Galactic center. We also note that the densest regions tend to be more compact (i.e., smaller in spatial extent) for the clumps in the outer Galaxy than for the clumps in the inner Galaxy. This is likely a consequence of the higher overall $H_2$ column densities found in the inner Galaxy (by more than a factor of 10) with respect to the outer Galaxy.

### 4.2. Mass-size relation

Kauffmann & Pillai (2010) found an empirical mass-size threshold above which massive star formation can occur using solar neighborhood clouds devoid of massive star formation. Regions forming massive stars must thus be, at a given radius, more massive than the limit mass ($m_{\rm lim}[r] = 870\ M_\odot [r/{\rm pc}]^{1.33}$). In Fig. 11, we show the mass-size diagram for the selected *Planck* cold clumps based on their *Herschel* data. Solid lines indicate the range of masses and radii for the sources with

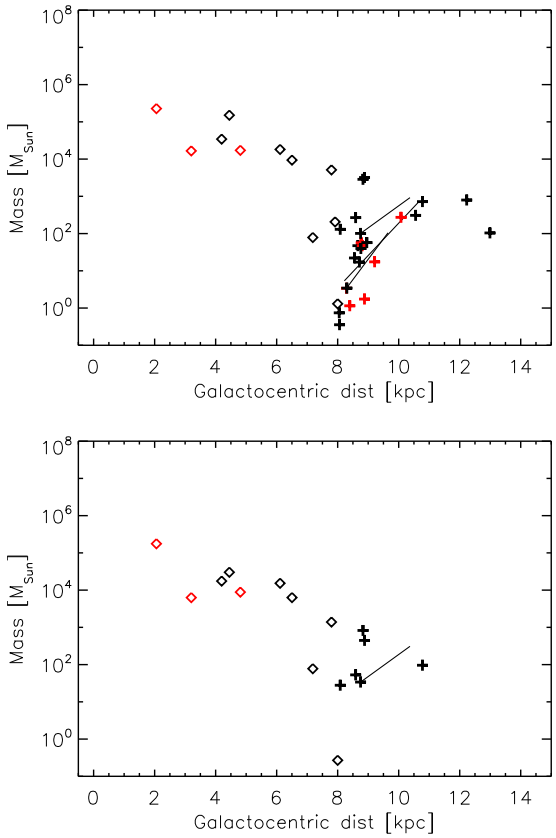


**Fig. 9.** Mass as a function of Galactocentric distance for the ECC Hi-GAL objects. Red and black symbols indicate the clumps from Category I and II, respectively. Plus signs indicate the clumps in the outer part of the Galaxy and diamonds indicate the sources in the inner Galaxy. Solid lines show the ranges of masses and Galactocentric distances for sources with large distance discrepancies. *Top*: calculated mass above $3 \times 10^{21}$ cm$^{-2}$. *Bottom*: mass of the high column density gas, $N(H_2) > 10^{22}$ cm$^{-2}$.

large distance discrepancies. They are all located below the empirical mass-size threshold of massive star formation. Twenty-five percent of the *Planck* ECC clumps in the Galactic Plane with *Herschel*-based derived masses have the potential to form massive stars since these masses lie above the mass limit proposed by Kauffmann & Pillai (2010). These ECC clumps are the most massive and also the largest in size among our sample, which is consistent with the idea that massive stars tend to form in the largest, most massive clumps (Wang et al. 2009). Their distances are very typical for the sample, between 1.1 kpc and 6.04 kpc. We note that three out of these clumps do not have 70 $\mu$m point sources (G006.96+00.89, G009.79+00.87, and G354.81+00.35), which makes them good candidates to study the earliest stages of star formation. Two of the sources above the mass limit are in the outer Galaxy (G224.27-00.82 and G224.47-00.65), but they contain 70 $\mu$m point sources already, which confirms their ability to form stars.

In addition, we can investigate the possible evolution of the mass of the clumps by calculating the ECC clump masses and sizes contained within five different $H_2$ column density thresholds: $10^{21}$, $3\times10^{21}$, $5\times10^{21}$, $8\times10^{21}$, and $10^{22}$ cm$^{-2}$. The bottom panel of Fig. 11 shows the mass-size relationship. The lines represent the evolution of the calculated values within the different thresholds. As shown in Fig. 11, the lines are almost parallel to the mass-size threshold. This demonstrates that the number of

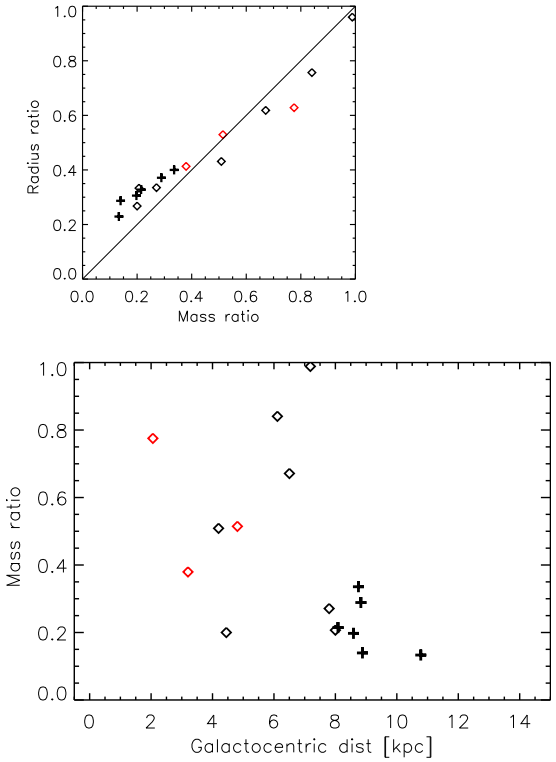


**Fig. 10.** *Top*: distribution of the size ratio [Size($10^{22}$ cm$^{-2}$)/Size($3 \times 10^{21}$ cm$^{-2}$)] as a function of the mass ratio [Mass($10^{22}$ cm$^{-2}$)/Mass($3 \times 10^{21}$ cm$^{-2}$)] for two different column density thresholds: $3 \times 10^{21}$ cm$^{-2}$ and $10^{22}$ cm$^{-2}$. *Bottom*: distribution of the mass ratio as a function of the Galactocentric distance. On both plots, red and black symbols indicate the clumps from Category I and II, respectively. Plus signs indicate the clumps in the outer part of the Galaxy and diamonds indicate the sources in the inner Galaxy.

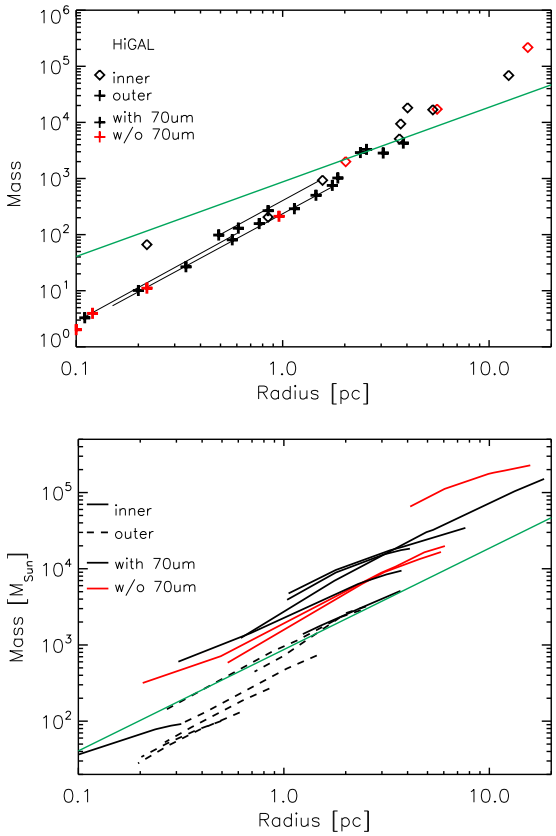


**Fig. 11.** *Top*: mass-size diagram for the ECC Hi-GAL objects based on the Hi-GAL *Herschel* column density maps. Sources with available distance estimates are shown. Red and black symbols indicate the clumps from Category I and II, respectively. Plus signs indicate the clumps in the outer part of the Galaxy and diamonds indicate the sources in the inner Galaxy. Green line indicates the mass-size threshold for massive star formation: $m_{\rm lim} = 870\ M_\odot (r/{\rm pc})^{1.33}$ (Kauffmann & Pillai 2010). Solid lines show the ranges of masses and radii for sources with large distance discrepancies. *Bottom*: mass-size diagram based on the Hi-GAL column density maps. Masses and sizes are calculated within different column density limits; see details in text. Sources with peak column density values larger than $10^{22}$ cm$^{-2}$ are shown. Dashed lines indicate the sources in the outer Galaxy. Red lines indicate the sources without 70 $\mu$m point sources.

sources with the potential to form high-mass stars does not depend on the selected column density threshold.

We stress that two clumps are found in the Outer Galaxy that fulfill the criteria of high-mass star formation. Their masses and sizes based on the *Planck* catalog information also fulfill this criteria. Three clumps without 70 $\mu$m emission are found above the high-mass star formation threshold in the inner Galaxy. These clumps represent good candidates to study the earliest phases of massive star and star cluster formation.

## 5. Summary

We investigate the basic physical properties of 48 *Planck* ECC clumps in the Galactic plane using *Herschel* Hi-GAL data. Starless (~22%) and star-forming (~78%) clumps were identified in the inner and outer part of the Galaxy. We calculated their masses and sizes based on background subtracted *Herschel* images, and we characterized their evolutionary stage based on the presence, or absence, of point-like 70 $\mu$m emission (an excellent probe of massive star formation). No clear difference was found in the mass and temperature of starless and star-forming clumps based on our data. *Planck* clumps located in the Galactic center show higher column densities and average dust temperatures than those located in the outer Galaxy. We identified five particularly interesting objects in the Galactic plane that are good candidates for higher resolution continuum and molecular line studies. Three of these objects (G006.96+00.89, G009.79+00.87, and G354.81+00.35) are located in the inner Galaxy, fulfill the criteria of massive star and star cluster formation, and show no 70 $\mu$m emission. These objects are thus excellent templates to study the earliest phases of massive star and star cluster formation. Two objects with 70 $\mu$m emission (G224.27-00.82 and G224.47-00.65) were found in the outer part of the Galaxy, which also fulfill the massive star formation criteria; with a follow-up study of these objects, the properties of massive star-forming clumps can be compared directly in the inner and outer part of the Galaxy.

*Acknowledgements.* This work has made use of the APLpy plotting package (https://aplpy.github.io/) and the agpy code package (https://pypi.python.org/pypi/agpy/0.1.4). K.W. acknowledges the support from Deutsche Forschungsgemeinschaft (DFG) grant WA3628-1/1 through priority program 1573 ("Physics of the Interstellar Medium"). I.J.-S. acknowledges the financial support received from the People Programme (Marie Curie Actions) of the European Union's Seventh Framework Programme (FP7/2007–2013) under REA grant agreement PIIF-GA-2011-301538 and from the STFC through an Ernest Rutherford Fellowship (proposal number ST/L004801/1). L.V.T. and S.Z. acknowledges support by the OTKA grants NN-111016 and K101393.

## References

Aguirre, J. E., Ginsburg, A. G., Dunham, M. K., et al. 2011, ApJS, 192, 4
Battersby, C., Bally, J., Ginsburg, A., et al. 2011, A&A, 535, A128
Bertin, E., & Arnouts, S. 1996, A&AS, 117, 393

Butler, M. J., & Tan, J. C. 2009, ApJ, 696, 484
Chambers, E. T., Jackson, J. M., Rathborne, J. M., & Simon, R. 2009, ApJS, 181, 360
Dame, T. M., Hartmann, D., & Thaddeus, P. 2001, ApJ, 547, 792
Dunham, M. M., Crapsi, A., Evans, II, N. J., et al. 2008, ApJS, 179, 249
Foster, J. B., Stead, J. J., Benjamin, R. A., Hoare, M. G., & Jackson, J. M. 2012, ApJ, 751, 157
Griffin, M. J., Abergel, A., Abreu, A., et al. 2010, A&A, 518, L3
Güver, T., & Özel, F. 2009, MNRAS, 400, 2050
Jackson, J. M., Finn, S. C., Rathborne, J. M., Chambers, E. T., & Simon, R. 2008, ApJ, 680, 349
Jackson, J. M., Rathborne, J. M., Foster, J. B., et al. 2013, PASA, 30, 57
Juvela, M., Ristorcelli, I., Pagani, L., et al. 2012, A&A, 541, A12
Kauffmann, J., & Pillai, T. 2010, ApJ, 723, L7
Kennicutt, R. C., & Evans, N. J. 2012, ARA&A, 50, 531
Longmore, S. N., Kruijssen, J. M. D., Bally, J., et al. 2013, MNRAS, 433, L15
Marton, G., Tóth, L. V., Paladini, R., et al. 2016, MNRAS, 458, 3479
Molinari, S. 2011, Herschel Space Observatory Proposal, 1899
Molinari, S. 2012, Herschel Space Observatory Proposal, 2454
Molinari, S., Swinyard, B., Bally, J., et al. 2010, PASP, 122, 314
Parsons, H., Thompson, M. A., & Chrysostomou, A. 2009, MNRAS, 399, 1506
Peretto, N., Fuller, G. A., Plume, R., et al. 2010, A&A, 518, L98
Pillai, T., Wyrowski, F., Carey, S. J., & Menten, K. M. 2006, A&A, 450, 569
Planck Collaboration XXIII. 2011, A&A, 536, A23
Planck Collaboration XXVIII. 2016, A&A, in press, DOI: 10.1051/0004-6361/201525819
Poglitsch, A., Waelkens, C., Geis, N., et al. 2010, A&A, 518, L2
Ragan, S., Henning, T., Krause, O., et al. 2012, A&A, 547, A49
Rathborne, J. M., Jackson, J. M., & Simon, R. 2006, ApJ, 641, 389
Rathborne, J. M., Lada, C. J., Muench, A. A., Alves, J. F., & Lombardi, M. 2008, ApJS, 174, 396
Reid, M. J., Menten, K. M., Zheng, X. W., et al. 2009, ApJ, 700, 137
Reid, M. J., Menten, K. M., Brunthaler, A., et al. 2014, ApJ, 783, 130
Schuller, F., Menten, K. M., Contreras, Y., et al. 2009, A&A, 504, 415
Tan, J. C., Kong, S., Butler, M. J., Caselli, P., & Fontani, F. 2013, ApJ, 779, 96
Tauber, J. A., Mandolesi, N., Puget, J.-L., et al. 2010, A&A, 520, A1
Tóth, L. V., Marton, G., Zahorecz, S., et al. 2014, PASJ, 66, 17
Veneziani, M., Elia, D., Noriega-Crespo, A., et al. 2013, A&A, 549, A130
Wang, K., Wu, Y. F., Ran, L., Yu, W. T., & Miller, M. 2009, A&A, 507, 369
Wang, K., Zhang, Q., Wu, Y., & Zhang, H. 2011, ApJ, 735, 64
Wang, K., Zhang, Q., Wu, Y., Li, H.-B., & Zhang, H. 2012, ApJ, 745, L30
Wang, K., Zhang, Q., Testi, L., et al. 2014, MNRAS, 439, 3275
Wang, K., Testi, L., Ginsburg, A., et al. 2015, MNRAS, 450, 4043
Wilcock, L. A., Ward-Thompson, D., Kirk, J. M., et al. 2012, MNRAS, 422, 1071
Wu, Y., Liu, T., Meng, F., et al. 2012, ApJ, 756, 76
Zhang, Q., Wang, K., Lu, X., & Jiménez-Serra, I. 2015, ApJ, 804, 141

## Appendix A: *Herschel* images of the clumps

In Figs. A.1–A.8, we show the *Herschel* 70, 250 and 500 $\mu$m images of the investigated *Planck* ECC objects (intensity scale in units of MJy/sr) with a resolution of 5″, 18″, and 36″. Black circles are centered at the positions of the *Planck* clumps and their sizes correspond to the derived major axis of the clumps.

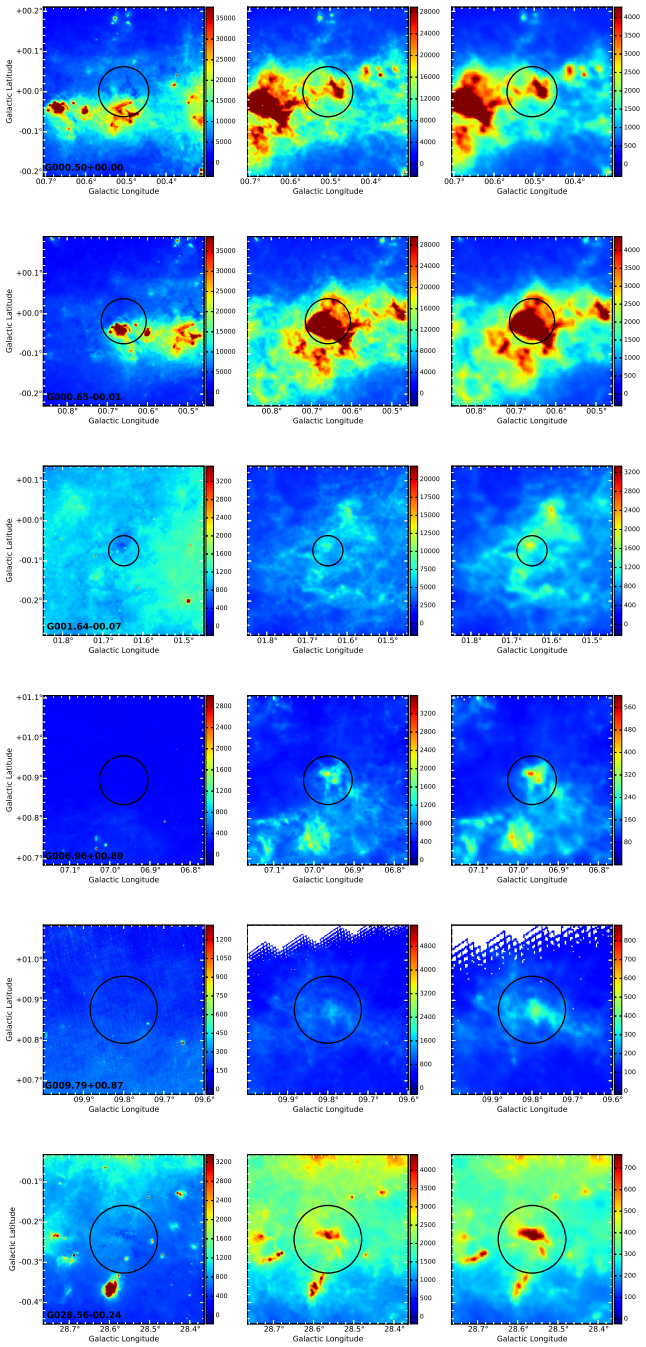


**Fig. A.1.** *Herschel* 70, 250, and 500 $\mu$m images of the selected *Planck* cold clumps given in units of MJy/sr with a resolution of 5″, 18″, and 36″. Black circles are centered at the positions of the *Planck* clumps and circle sizes correspond to the derived major axis of the clumps.

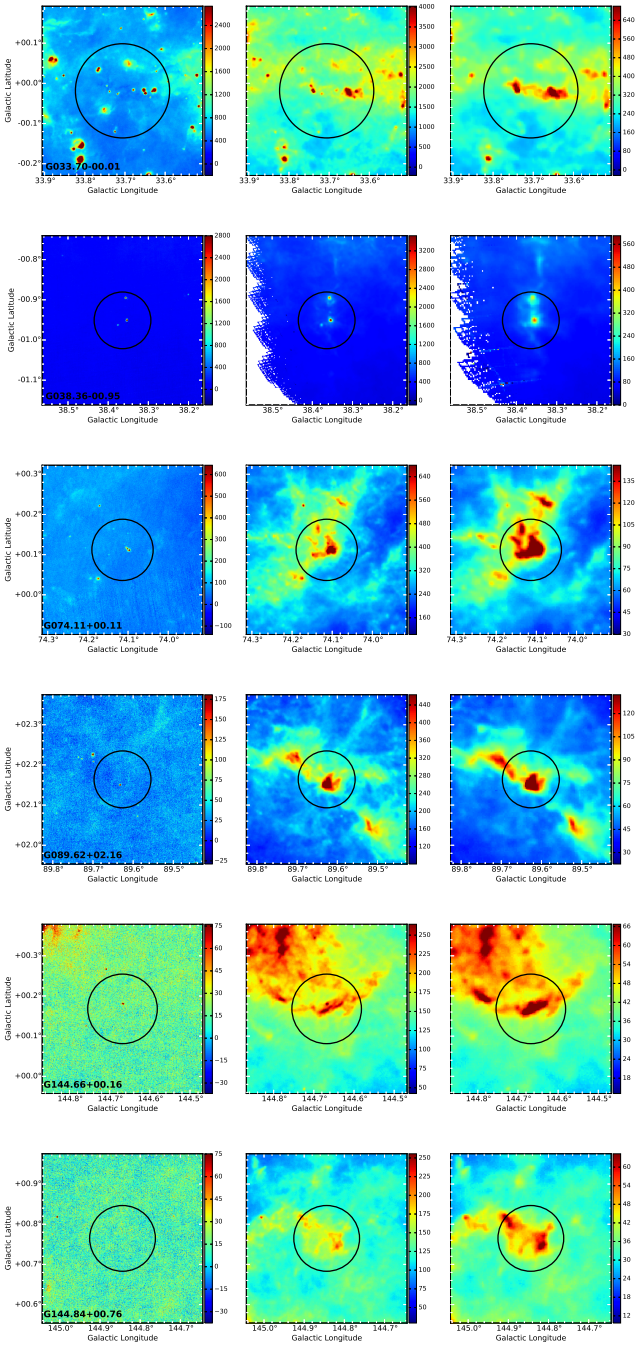


**Fig. A.2.** *Herschel* 70, 250, and 500 $\mu$m images of the selected *Planck* cold clumps given in units of MJy/sr with a resolution of 5″, 18″, and 36″. Black circles are centered at the positions of the *Planck* clumps and circle sizes correspond to the derived major axis of the clumps.

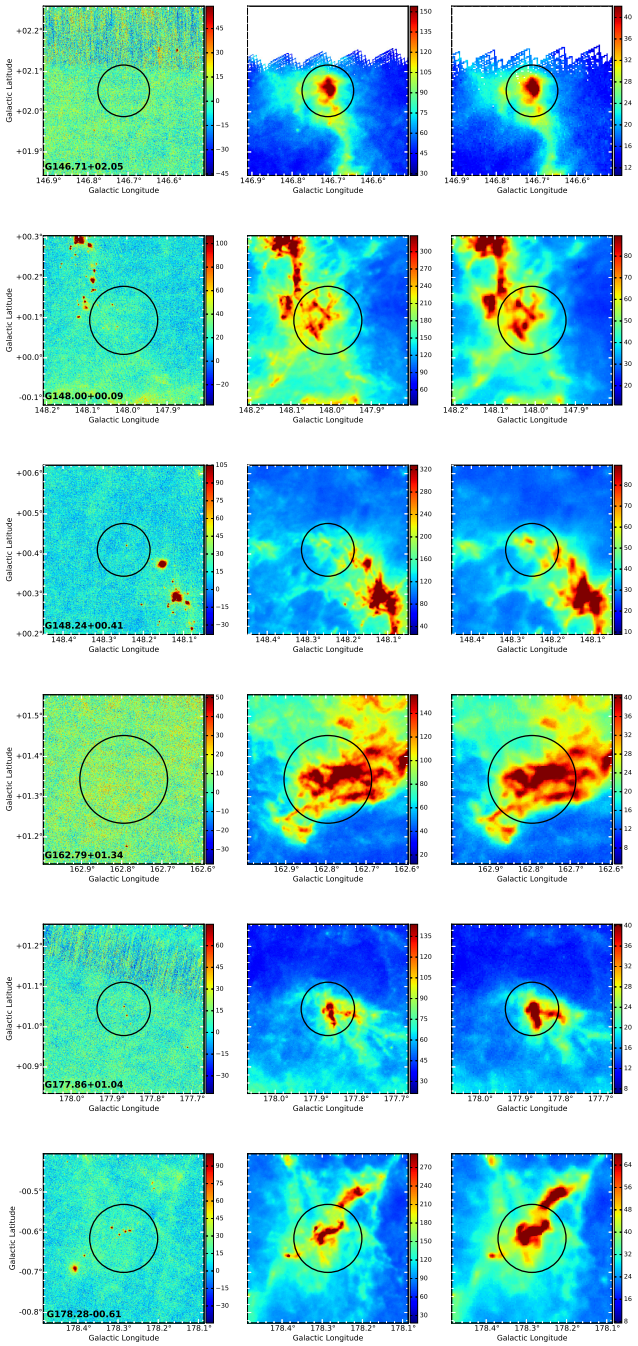


**Fig. A.3.** *Herschel* 70, 250, and 500 $\mu$m images of the selected *Planck* cold clumps given in units of MJy/sr with a resolution of 5″, 18″, and 36″. Black circles are centered at the positions of the *Planck* clumps and circle sizes correspond to the derived major axis of the clumps.

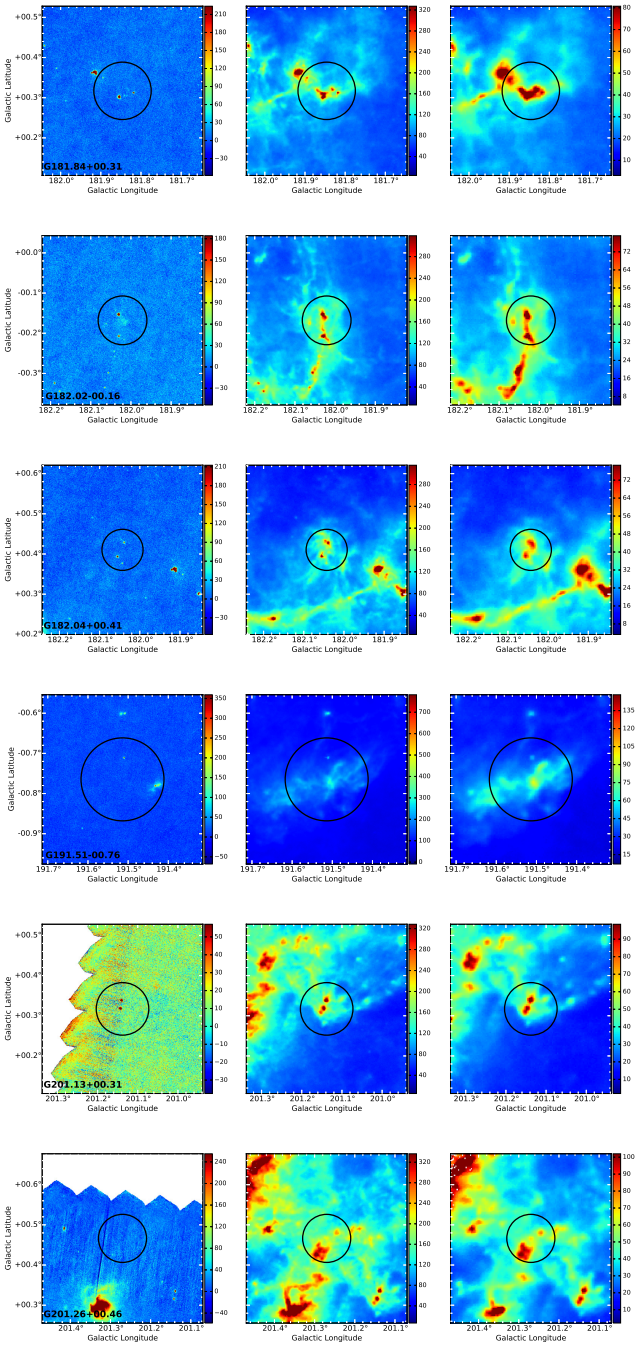


**Fig. A.4.** *Herschel* 70, 250, and 500 $\mu$m images of the selected *Planck* cold clumps given in units of MJy/sr with a resolution of 5″, 18″, and 36″. Black circles are centered at the positions of the *Planck* clumps and circle sizes correspond to the derived major axis of the clumps.

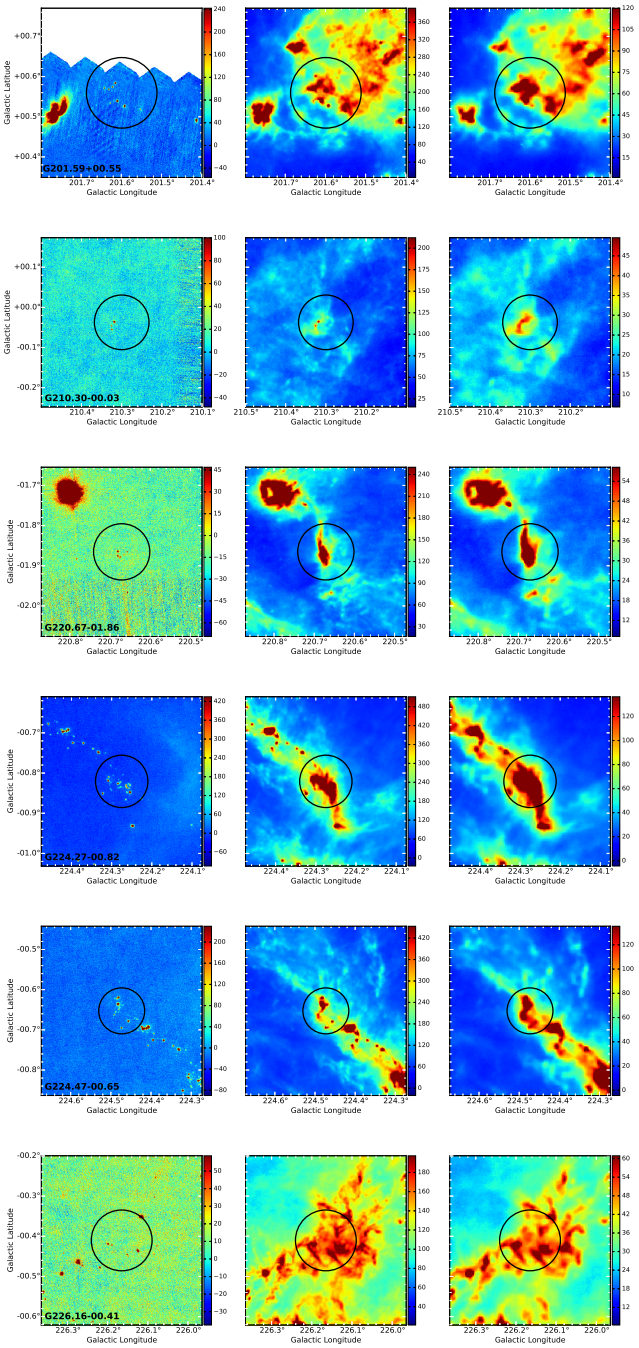


**Fig. A.5.** *Herschel* 70, 250, and 500 $\mu$m images of the selected *Planck* cold clumps given in units of MJy/sr with a resolution of 5″, 18″, and 36″. Black circles are centered at the positions of the *Planck* clumps and circle sizes correspond to the derived major axis of the clumps.

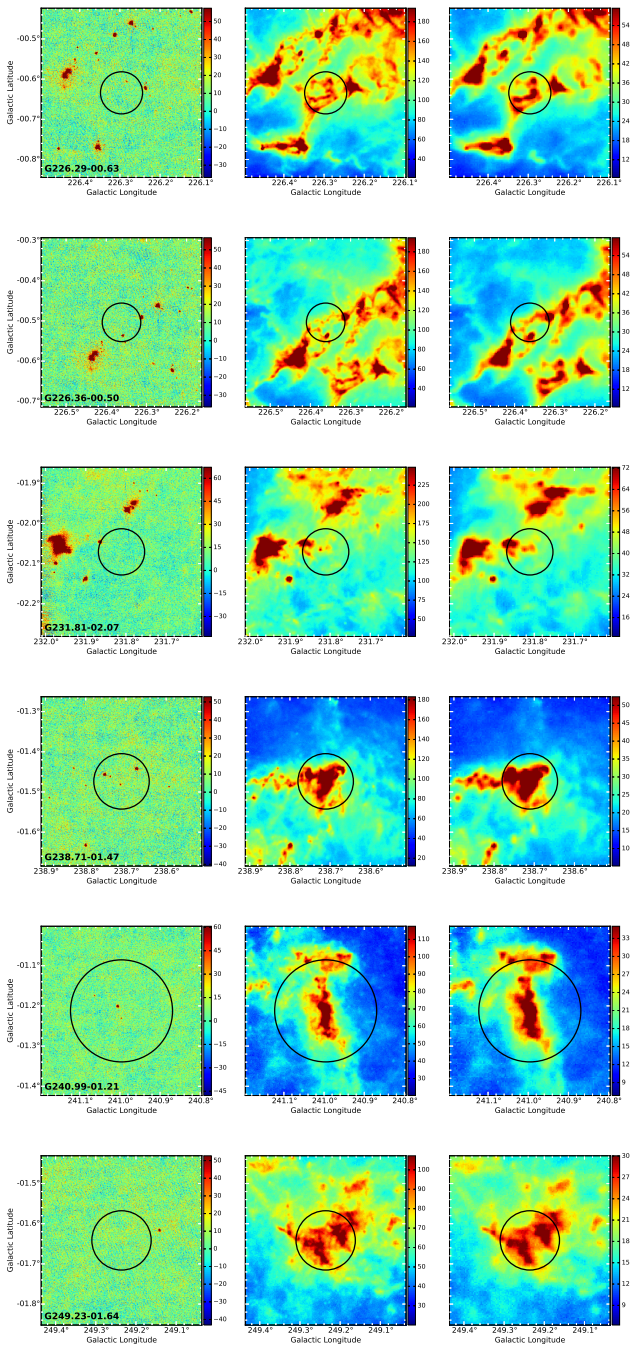


**Fig. A.6.** *Herschel* 70, 250, and 500 $\mu$m images of the selected *Planck* cold clumps given in units of MJy/sr with a resolution of 5″, 18″, and 36″. Black circles are centered at the positions of the *Planck* clumps and circle sizes correspond to the derived major axis of the clumps.

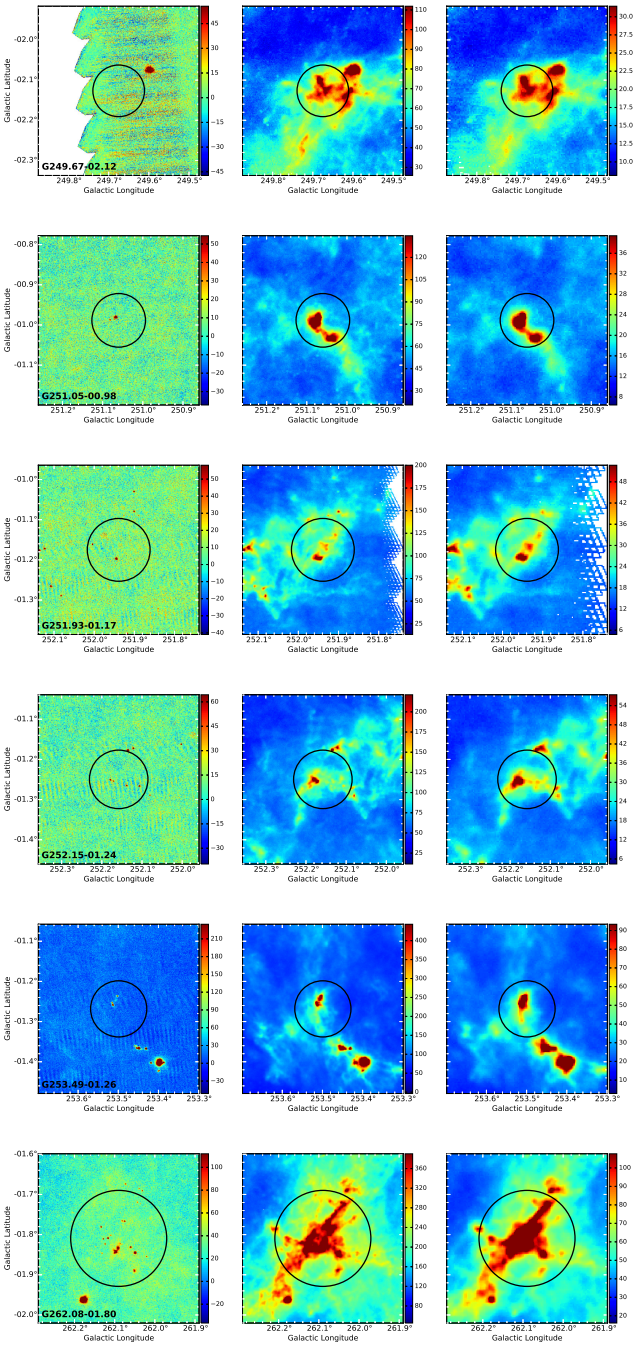


**Fig. A.7.** *Herschel* 70, 250, and 500 $\mu$m images of the selected *Planck* cold clumps given in units of MJy/sr with a resolution of 5″, 18″, and 36″. Black circles are centered at the positions of the *Planck* clumps and circle sizes correspond to the derived major axis of the clumps.

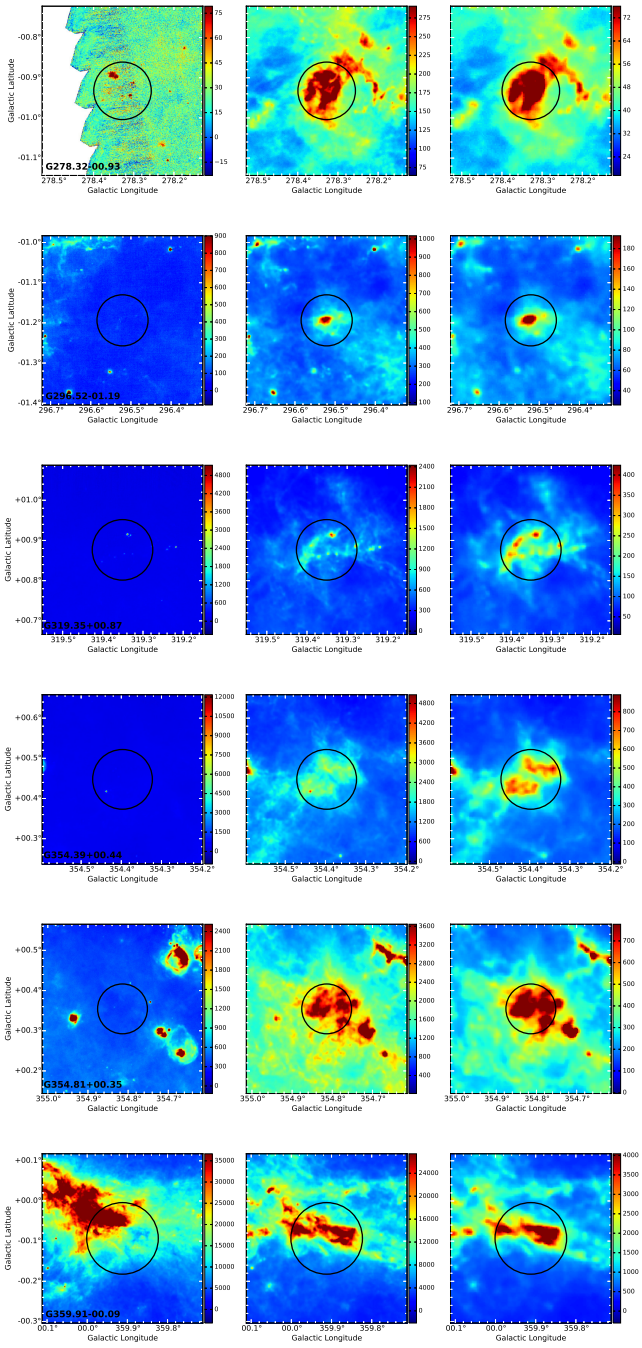


**Fig. A.8.** *Herschel* 70, 250, and 500 $\mu$m images of the selected *Planck* cold clumps given in units of MJy/sr with a resolution of 5″, 18″, and 36″. Black circles are centered at the positions of the *Planck* clumps and circle sizes correspond to the derived major axis of the clumps.

**Table A.1.** Calculated T, M, R for the ECC clumps.

| Name | Distance [kpc] | $T_{ECC}$ [K] | major$_{ECC}$ [′] | $R_{ECC}$ [pc] | $M_{ECC}$ [$M_\odot$] | Max $N(H_2)$ [cm$^{-2}$] | $T_{N\geq10^{22}}$ [k] | $M_{N\geq10^{22}}$ [$M_\odot$] | $R_{N\geq10^{22}}$ [pc] | $T_{N\geq3\times10^{21}}$ [K] | $M_{N\geq3\times10^{21}}$ [$M_\odot$] | $R_{N\geq3\times10^{21}}$ [pc] | Category |
|---|---|---|---|---|---|---|---|---|---|---|---|---|---|
| G000.50+00.00 | 7.40[6] | 9.49 | 7.48 | 8.05 | 5.45E+06 | 2.03E+24 | | | | | | | II |
| G000.65-00.01 | 8.09[2] | 8.91 | 6.73 | 7.91 | 2.73E+07 | 7.40E+24 | | | | | | | II |
| G001.64-00.07 | 7.39[2] | 9.59 | 4.51 | 4.85 | 1.21E+06 | 2.65E+23 | | | | | | | II |
| G006.96+00.89 | 4.89[1] | 9.29 | 7.27 | 5.17 | 1.14E+04 | 1.22E+23 | 12.95 | 6.30E+03 | 2.40 | 12.91 | 1.66E+04 | 5.81 | I |
| G009.79+00.87 | 3.27[4] | 9.24 | 10.02 | 4.76 | 8.31E+04 | 2.62E+23 | 12.20 | 8.85E+03 | 2.97 | 12.74 | 1.72E+04 | 5.61 | I |
| G028.56-00.24 | 5.30[6] | 12.37 | 10.1 | 7.78 | 4.85E+04 | 1.05E+23 | 13.76 | 1.75E+04 | 3.29 | 15.10 | 3.44E+04 | 7.63 | II |
| G033.70-00.01 | 6.94[1] | 12.11 | 14.07 | 14.19 | 1.53E+05 | 6.22E+22 | 14.77 | 3.02E+04 | 4.94 | 19.08 | 1.51E+05 | 18.46 | II |
| G038.36-00.95 | 1.08[1] | 9.28 | 8.47 | 1.33 | 4.28E+03 | 1.70E+23 | 10.98 | 7.76E+01 | 0.24 | 10.98 | 7.85E+01 | 0.25 | II |
| G074.11+00.11 | 3.45[5] | 9.14 | 9.15 | 4.59 | 2.80E+04 | 3.05E+22 | 12.39 | 1.39E+03 | 1.24 | 12.77 | 5.13E+03 | 3.70 | II |
| G089.62+02.16 | 0.06[1] | 8.35 | 8.5 | 0.07 | 1.06E+01 | 2.61E+22 | 11.82 | 2.69E-01 | 0.02 | 12.18 | 1.30E+00 | 0.06 | II |
| G144.66+00.16 | 0.35[1] | 13.94 | 10.39 | 0.53 | 2.05E+01 | 8.58E+21 | | | | 12.01 | 3.39E+00 | 0.11 | I |
| G144.84+00.76 | 2.42[1] | 8.23 | 9.82 | 3.45 | 6.08E+03 | 8.42E+21 | | | | 10.97 | 2.73E+02 | 1.09 | I |
| G146.71+02.05 | 1.03[6] | 11.14 | 7.71 | 1.15 | 3.67E+02 | 3.21E+21 | | | | 13.70 | 1.74E+00 | 0.10 | I |
| G148.00+00.09 | 0.77[6] | 13.13 | 10.16 | 1.14 | 1.48E+02 | 6.33E+21 | | | | 13.46 | 4.73E+01 | 0.45 | II |
| G148.24+00.41 | 3.12[1] | 11.97 | 7.88 | 3.57 | 2.13E+03 | 2.74E+22 | 6.61 | 9.60E+01 | 0.33 | 9.29 | 7.21E+02 | 1.44 | II |
| G162.79+01.34 | 1.26[6] | 11.82 | 13.1 | 2.40 | 6.74E+02 | 4.57E+21 | | | | 14.12 | 1.74E+01 | 0.29 | I |
| G177.86+01.04 | 0.30[6] | 12.52 | 7.97 | 0.35 | 1.32E+01 | 8.75E+21 | | | | 11.07 | 3.42E+00 | 0.11 | II |
| G178.28-00.61 | | 9.32 | 10.16 | | | 1.16E+22 | 12.84 | | | 13.32 | | | II |
| G181.84+00.31 | | 10.80 | 8.57 | | | 1.16E+22 | 13.36 | | | 12.33 | | | II |
| G182.02-00.16 | | 12.55 | 7.27 | | | 6.50E+21 | | | | 13.40 | | | II |
| G182.04+00.41 | | 11.19 | 6.14 | | | 5.87E+21 | | | | 12.36 | | | II |
| G191.51-00.76 | 0.82[6] | 11.54 | 12.39 | 1.48 | 3.55E+02 | 6.96E+21 | | | | 13.21 | 4.70E+01 | 0.44 | I |
| G201.13+00.31 | 0.76[1] | 15.08 | 7.85 | 0.87 | 1.37E+02 | 8.45E+21 | | | | 13.21 | 1.71E+01 | 0.25 | II |
| G201.26+00.46 | 0.82[1] | 18.39 | 7.18 | 0.86 | 4.93E+01 | 8.46E+21 | | | | 12.55 | 5.65E+01 | 0.43 | I |
| G201.59+00.55 | 0.63[6] | 10.31 | 10.54 | 0.97 | 5.71E+02 | 1.85E+22 | 12.18 | 5.29E+01 | 0.26 | 12.70 | 2.68E+02 | 0.85 | II |
| G210.30-00.03 | 5.44[6] | 10.78 | 8.16 | 6.45 | 3.47E+03 | 4.00E+21 | | | | 11.50 | 1.04E+02 | 0.71 | II |
| G220.67-01.86 | 0.96[1] | 14.39 | 8.4 | 1.17 | 1.60E+02 | 1.85E+22 | 11.92 | 3.39E+01 | 0.20 | 11.87 | 1.01E+02 | 0.50 | II |
| G224.27-00.82 | 1.11[1] | 11.72 | 7.82 | 1.26 | 2.06E+03 | 7.80E+22 | 12.09 | 8.26E+02 | 0.88 | 11.68 | 2.86E+03 | 2.37 | II |
| G224.47-00.65 | 1.18[1] | 9.32 | 6.86 | 1.18 | 3.15E+03 | 6.20E+22 | 12.10 | 4.46E+02 | 0.72 | 11.73 | 3.20E+03 | 2.51 | II |
| G226.16-00.41 | 1.05[6] | 11.29 | 9.08 | 1.39 | 3.29E+02 | 5.55E+21 | | | | 13.03 | 3.97E+01 | 0.43 | II |
| G226.29-00.63 | 1.31[1] | 11.65 | 6.29 | 1.20 | 1.41E+02 | 5.98E+21 | | | | 12.07 | 5.72E+01 | 0.49 | II |
| G226.36-00.50 | 0.77[6] | 11.28 | 5.76 | 0.64 | 1.29E+02 | 8.20E+21 | | | | 12.25 | 2.21E+01 | 0.30 | II |
| G231.81-02.07 | 3.53[6] | 13.97 | 6.91 | 3.55 | 1.72E+03 | 5.79E+21 | | | | 12.64 | 3.08E+02 | 1.17 | II |
| G238.71-01.47 | | 11.48 | 8.28 | | | 9.49E+21 | | | | 12.82 | | | II |
| G240.99-01.21 | 6.15[6] | 10.78 | 15.24 | 13.63 | 1.20E+04 | 6.84E+21 | | | | 12.97 | 7.95E+02 | 1.80 | II |
| G249.23-01.64 | 1.08[4] | 11.66 | 8.86 | 1.39 | 2.03E+02 | 1.85E+21 | | | | | | | I |
| G249.67-02.12 | 0.99[4] | 9.25 | 7.71 | 1.11 | 5.12E+02 | 3.67E+21 | | | | 12.31 | 1.15E+00 | 0.08 | I |
| G251.05-00.98 | | 12.81 | 8.01 | | | 7.47E+21 | | | | 12.32 | | | II |
| G251.93-01.17 | 0.19[4] | 10.34 | 9.38 | 0.26 | 1.81E+01 | 5.81E+21 | | | | 12.86 | 3.56E-01 | 0.04 | II |
| G252.15-01.24 | 0.16[4] | 9.92 | 8.74 | 0.20 | 1.30E+01 | 8.64E+21 | | | | 11.94 | 7.43E-01 | 0.05 | II |
| G253.49-01.26 | | 11.23 | 8.39 | | | 1.23E+22 | 12.86 | | | 13.05 | | | II |
| G262.08-01.80 | 0.50[4] | 8.67 | 14.34 | 1.04 | 8.79E+02 | 2.05E+22 | 12.37 | 2.79E+01 | 0.20 | 13.23 | 1.30E+02 | 0.61 | II |
| G278.32-00.93 | 1.21[4] | 12.37 | 8.59 | 1.51 | 6.70E+02 | 9.05E+21 | | | | 13.38 | 2.06E+02 | 0.85 | II |
| G296.52-01.19 | | 14.47 | 7.63 | | | 2.20E+22 | 13.85 | | | 13.58 | | | II |
| G319.35+00.87 | 2.18[6] | 11.59 | 9.04 | 2.86 | 8.09E+03 | 4.32E+23 | 10.47 | 6.31E+03 | 2.30 | 10.85 | 9.40E+03 | 3.72 | II |
| G354.39+00.44 | 1.90[6] | 12.08 | 8.92 | 2.46 | 2.22E+04 | 5.06E+23 | 12.90 | 1.53E+04 | 3.05 | 13.14 | 1.82E+04 | 4.03 | II |
| G354.81+00.35 | 6.04[2] | 9.46 | 7.44 | 6.53 | 8.12E+05 | 9.86E+22 | 14.19 | 1.76E+05 | 9.90 | 14.85 | 2.27E+05 | 15.76 | I |
| G359.91-00.09 | 7.93[2] | 9.04 | 10.69 | 12.32 | 1.15E+07 | 2.03E+24 | | | | | | | II |

**Notes.** Flag in the distance column: [(1)] kinematic distance from Wu et al. (2012); [(2)] kinematic distance based on the MALT90 survey data; [(3)] kinematic distance based on APEX observations; [(4)] kinematic distance based on CfA survey data; [(5)] associations with known IRDCs and molecular cloud cores; and [(6)] distance estimate from the *Planck* PGCC Catalogue.

## Appendix B: Available distance estimates for the clumps

Table B.1 shows all the available estimated distances for the ECC objects, see the detailed description in Sect. 2.3.

**Table B.1.** Estimated distances for the ECC clumps.

| Name | Wu et al. 2012 | | MALT90 | | APEX | | CfA | | IRDC | | PGCC |
|---|---|---|---|---|---|---|---|---|---|---|---|
| | $V_{LSR}$ $^{13}CO$ [km s$^{-1}$] | $D$ [kpc] | $V_{LSR}$ $N_2H^+$ [km s$^{-1}$] | $D$ [kpc] | $V_{LSR}$ $^{13}CO$ [km s$^{-1}$] | $D$ [kpc] | $V_{LSR}$ $^{12}CO$ [km s$^{-1}$] | $D$ [kpc] | Name | $D$ [kpc] | [kpc] |
| G000.50+00.00 | | | 42.24 | 7.93/8.70 | | | | | | | 7.4 (4) |
| G000.65-00.01 | | | 85.76 | 8.09/8.57 | | | | | | | |
| G001.64-00.07 | | | 54.25 | 7.39/9.19 | | | | | G001.62-00.08 | | |
| G006.96+00.89 | 41.53 | 4.89/11.39 | | | | | 43 | 4.97 /11.33 | G006.95+00.88 | | |
| G009.79+00.87 | | | | | | | 27.2 | 3.27/12.75 | | | |
| G028.56-00.24 | 86.66 | 4.74/9.77 | | | | | | | G028.53-00.25 | 5.7 | 5.3 (4) |
| G033.70-00.01 | 105.89 | 6.94 | | | | | | | G033.69-00.01 | 7.1 | 7.1 (1) |
| G038.36-00.95 | 16.69 | 1.08/11.74 | | | | | 15.8 | 1.02/11.8 | G038.35-00.90 | | 1.2 (1) |
| G074.11+00.11 | −1.42 | 4.4/4.6 | | | | | | | | | 3.45 (5) |
| G089.62+02.16 | −0.34 | 0.06 | | | | | −0.8 | 0.05 | | | |
| G144.66+00.16 | −7.68 | 0.35 | | | | | −8.6 | 0.42 | | | |
| G144.84+00.76 | −30.55 | 2.42 | | | | | −31.2 | 2.49 | | | |
| G146.71+02.05 | 2.52 | | | | | | 0.8 | | | | −1.03 (5) |
| G148.00+00.09 | −6.40 | 0.26 | | | | | −33.8 | 3 | | | 0.77 (5) |
| G148.24+00.41 | −34.56 | 3.12 | | | | | −34.1 | 3.07 | | | |
| G162.79+01.34 | 1.36 | | | | | | 0 | | | | −1.26 (5) |
| G177.86+01.04 | −18.36 | | | | | | −18.9 | 1.66 | | | 0.3 (2) |
| G178.28-00.61 | | | | | | | 0.04 | | | | |
| G181.84+00.31 | 3.30 | | | | | | | | | | |
| G182.02-00.16 | 3.96 | | | | | | | | | | |
| G182.04+00.41 | 2.91 | | | | | | | | | | |
| G191.51-00.76 | 0.13 | 0.41 | | | | | | | | | −0.82 (5) |
| G201.13+00.31 | 5.08 | 0.76 | | | | | 7.4 | 1.04 | | | |
| G201.26+00.46 | 5.60 | 0.82 | | | | | 7.6 | 1.06 | | | |
| G201.59+00.55 | 4.42 | 0.66 | | | | | 7.5 | 1.03 | | | 0.63 (2) |
| G210.30-00.03 | 36.47 | 4.24 | | | | | | | | | 5.44 (5) |
| G220.67-01.86 | 12.11 | 0.96 | | | | | 33.4 | 2.9 | | | |
| G224.27-00.82 | 14.39 | 1.11 | | | | | | | | | |
| G224.47-00.65 | 15.34 | 1.18 | | | | | | | | | |
| G226.16-00.41 | 15.95 | 1.22 | | | | | | | | | 1.05 (5) |
| G226.29-00.63 | 17.19 | 1.31 | | | | | | | | | |
| G226.36-00.50 | 14.96 | 1.14 | | | | | | | | | 0.77 (5) |
| G231.81-02.07 | 42.43 | 3.46 | | | | | | | | | 3.53 (5) |
| G240.99-01.21 | | | | | | | | | | | 6.15 (5) |
| G249.23-01.64 | | | | | | | 11.84 | 1.08 | | | |
| G249.67-02.12 | | | | | | | 10.7 | 0.99 | | | |
| G251.93-01.17 | | | | | | | 2.6 | 0.19 | | | |
| G252.15-01.24 | | | | | | | 2.4 | 0.16 | | | |
| G262.08-01.80 | | | | | | | 3.7 | 0.5 | | | |
| G278.32-00.93 | | | | | | | −28.6 | 1.21 | | | |
| G319.35+00.87 | | | | | −34.22 | 2.9/9.95 | −40.5 | 2.7/10.15 | | | 2.18 (5) |
| G354.39+00.44 | | | | | 72.39 | 4.43/11.76 | | | G354.42+00.46 | | 1.9 (4) |
| G354.81+00.35 | | | 100.79 | 6.04/10.41 | | | | | G354.84+00.31 | | |
| G359.91-00.09 | | | 10.58 | 7.93/8.57 | | | | | G359.87-00.09 | 8 | |

**Notes.** The distance determination available in the PGCC catalog has been obtained by using different methods. The final number in parenthesis corresponds to: 1) kinematic distance estimates, 2) optical extinction based on SDSS DR7, 3) near-IR extinction toward IRDCs, and 4) near-IR extinction. In case of the near-IR extinction methods, negative values indicate the upper limits.

## Appendix C: Background subtraction

For the precise determination of clump masses and sizes, we have to subtract the background and foreground emission in the observed images. Different methods are available to perform this task: (i) the Fourier transform (FT) method, which separates the large-scale and small-scale structures (Wang et al. 2015); (ii) to use a reference, relatively emission-free region to derive a constant background value (Juvela et al. 2012); and iii) to perform the Gaussian fitting of the Galactic background along the Galactic latitude (Battersby et al. 2011).

For the background subtraction, we used $2^\circ \times 2^\circ$ maps around the central positions of the *Planck* cold clumps. These maps are much larger than the structures of interest. We smoothed all intensity images to the same resolution of $5'$ and used the smoothed map as background. In contrast to methods (ii) and (iii), this technique allows spatial variations in the background values across the maps. After background subtraction, the derived column densities are 15−20% lower and the dust temperatures are 1−3 K lower. We compared our method with the FT method introduced by Wang et al. (2015). Our column density values are in good agreement with the FT method, and the difference is on average only ∼10%. We caution, however, that this may be partly because of the specific properties of the power spectrum of the Hi-GAL images in large tiles, as both works have found; the same may not apply for other images with a different power spectrum characterization. Calculated dust temperature and column density maps based on the background subtracted maps are shown in Appendix D.

## Appendix D: $T_{dust}$ and $N(H_2)$ maps

Figures D.1–D.8 shows the *Herschel* 70 $\mu$m images ([MJy/sr], left panels), the calculated column density ([cm$^{-2}$], middle panels) in logarithmic scale, and the dust temperature maps ([K], right panels) for the ECC sources with a resolution of 36″. The calculation was based on the background subtracted *Herschel* 160–500 $\mu$m images. Black circles show the location (central position) and size (major axis given in the ECC catalog) of the *Planck* clumps. Yellow and red contour levels refer to the $H_2$ column density thresholds of $3 \times 10^{21}$ and $10^{22}$ cm$^{-2}$, respectively.

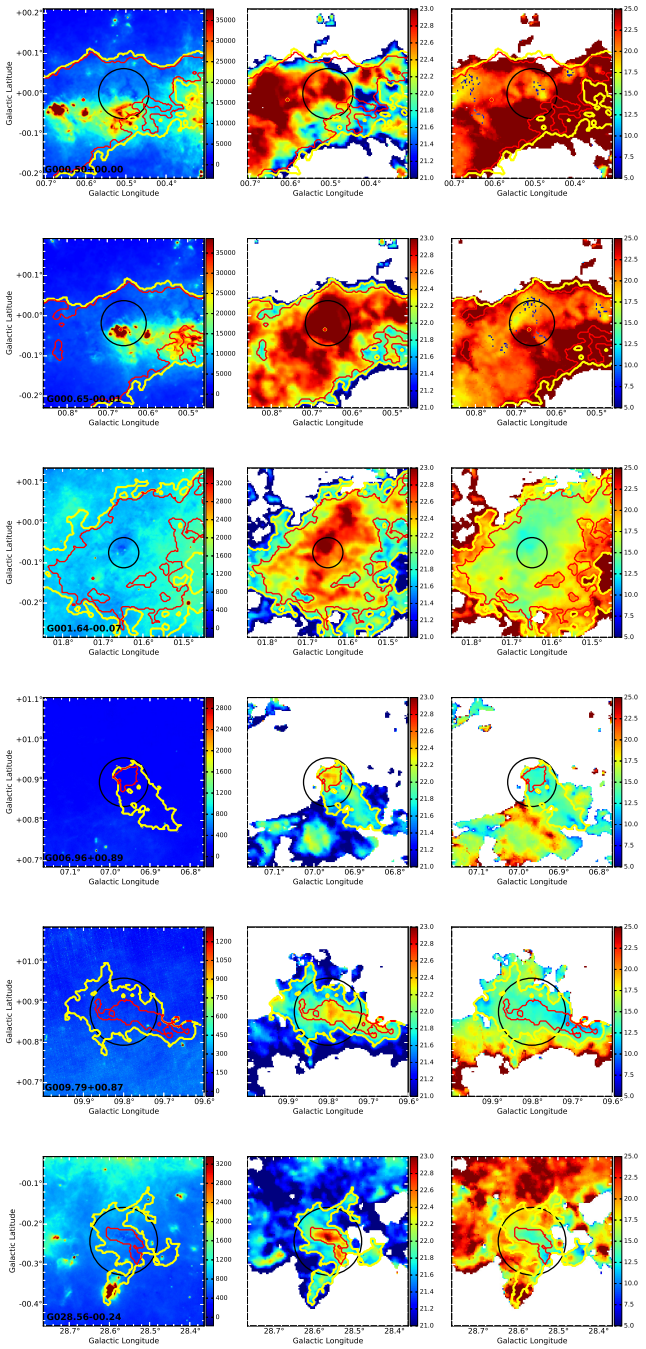


**Fig. D.1.** 70 $\mu$m images ([MJy/sr], *left*) and calculated column density ([cm$^{-2}$], *middle*) in logarithmic scale and dust temperature ([K], *right*) maps with a resolution of 36″. Yellow and red contour levels are at $3 \times 10^{21}$ cm$^{-2}$ and $10^{22}$ cm$^{-2}$, respectively. Black circles are placed at the positions of the *Planck* clumps and their sizes correspond to the major axis of the clumps reported in the ECC catalog.

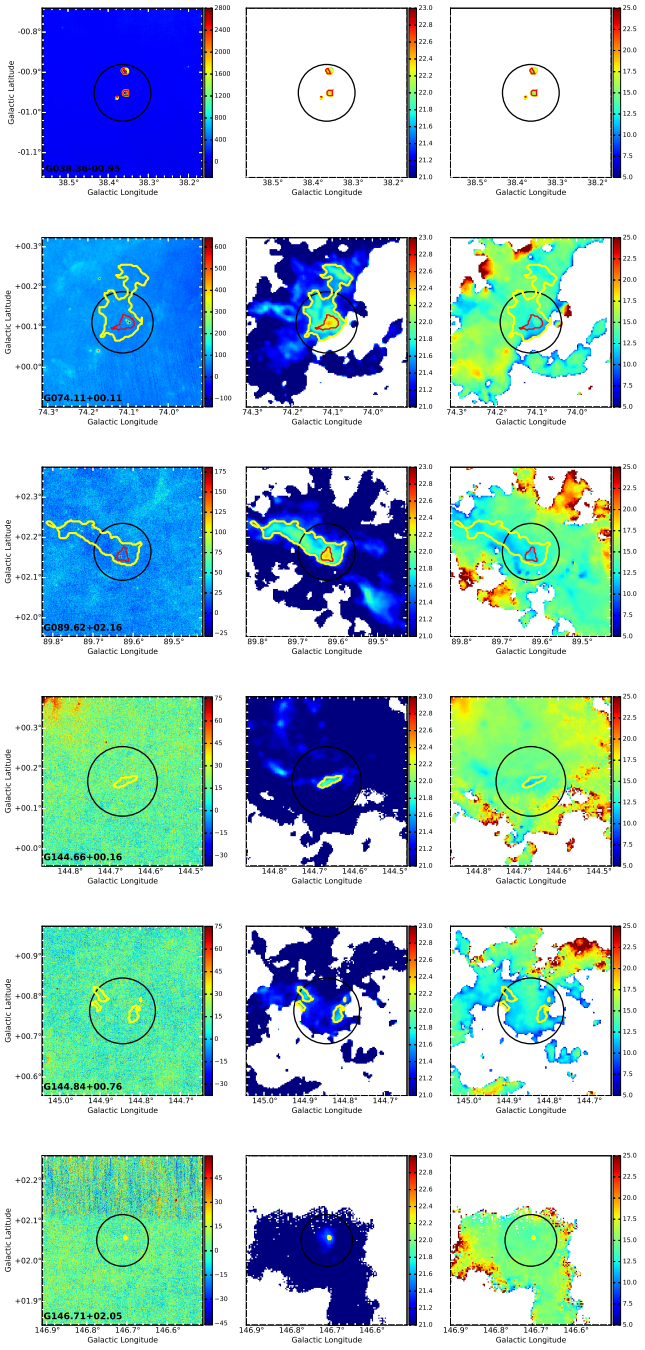


**Fig. D.2.** 70 $\mu$m images ([MJy/sr], *left*) and calculated column density ([cm$^{-2}$], *middle*) in logarithmic scale and dust temperature ([K], *right*) maps with a resolution of 36″. Yellow and red contour levels are at $3 \times 10^{21}$ cm$^{-2}$ and $10^{22}$ cm$^{-2}$, respectively. Black circles are placed at the positions of the *Planck* clumps and their sizes correspond to the major axis of the clumps reported in the ECC catalog.

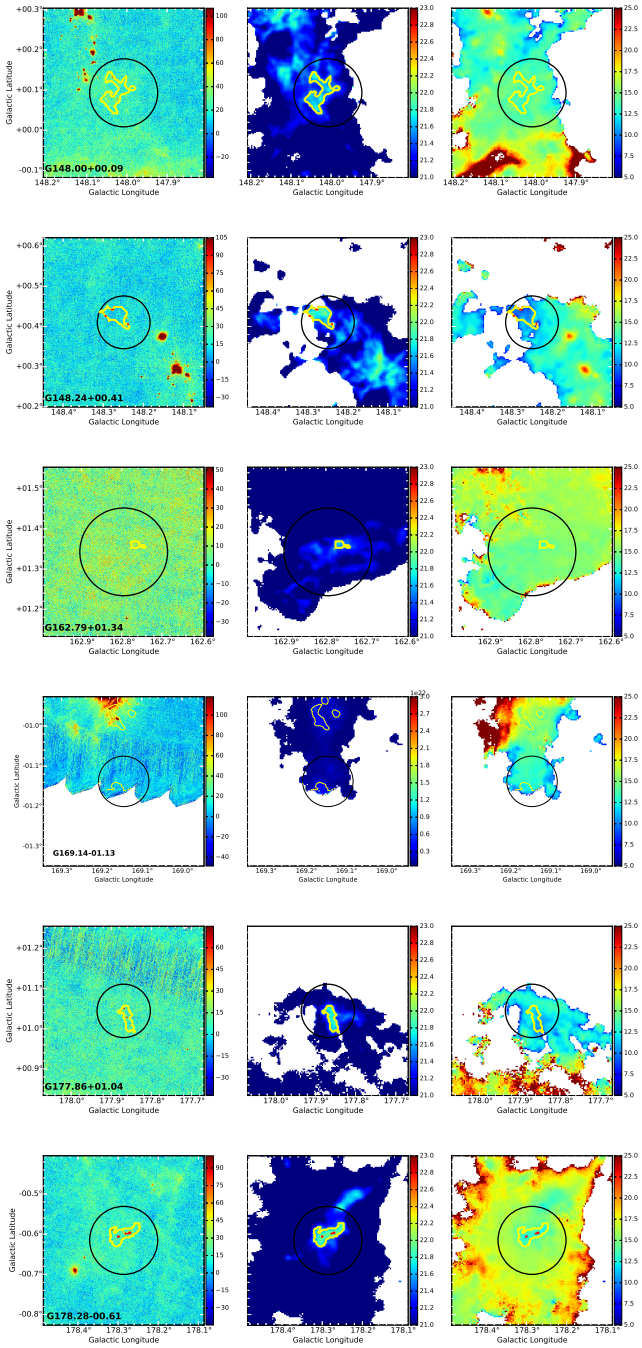


**Fig. D.3.** 70 $\mu$m images ([MJy/sr], *left*) and calculated column density ([cm$^{-2}$], *middle*) in logarithmic scale and dust temperature ([K], *right*) maps with a resolution of 36″. Yellow and red contour levels are at $3 \times 10^{21}$ cm$^{-2}$ and $10^{22}$ cm$^{-2}$, respectively. Black circles are placed at the positions of the *Planck* clumps and their sizes correspond to the major axis of the clumps reported in the ECC catalog.

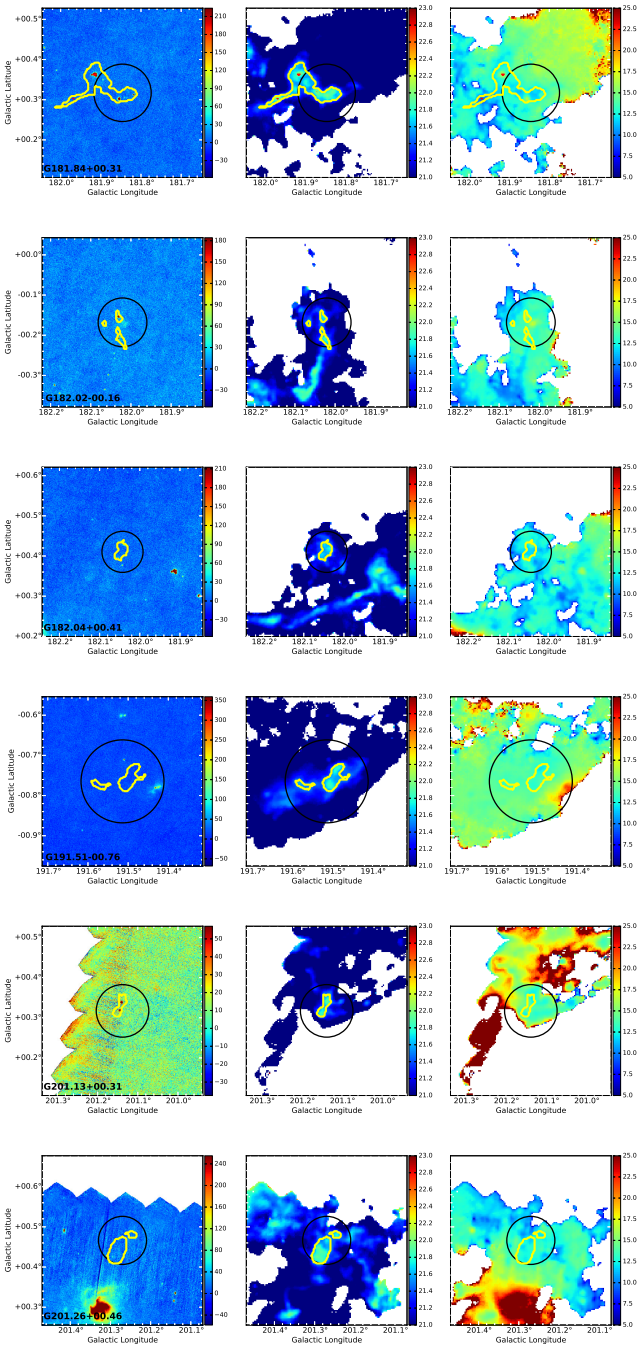


**Fig. D.4.** 70 $\mu$m images ([MJy/sr], *left*) and calculated column density ([cm$^{-2}$], *middle*) in logarithmic scale and dust temperature ([K], *right*) maps with a resolution of 36″. Yellow and red contour levels are at $3 \times 10^{21}$ cm$^{-2}$ and $10^{22}$ cm$^{-2}$, respectively. Black circles are placed at the positions of the *Planck* clumps and their sizes correspond to the major axis of the clumps reported in the ECC catalog.

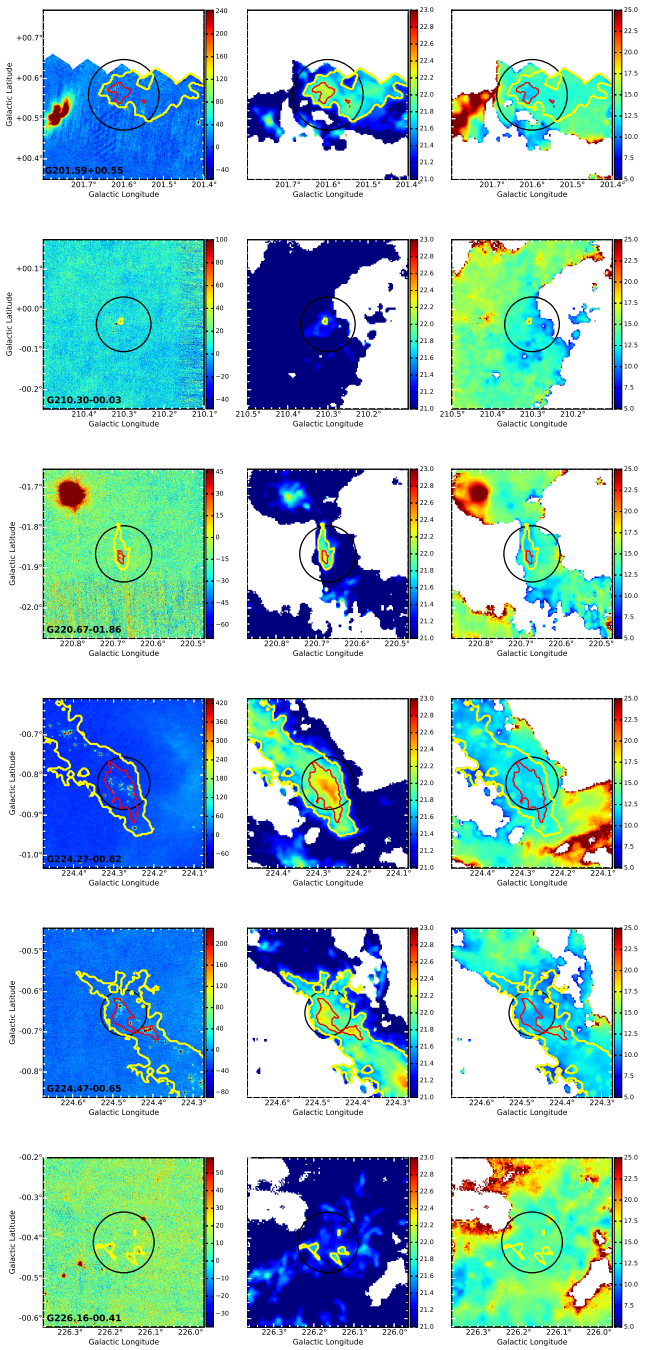


**Fig. D.5.** 70 $\mu$m images ([MJy/sr], *left*) and calculated column density ([cm$^{-2}$], *middle*) in logarithmic scale and dust temperature ([K], *right*) maps with a resolution of 36″. Yellow and red contour levels are at $3 \times 10^{21}$ cm$^{-2}$ and $10^{22}$ cm$^{-2}$, respectively. Black circles are placed at the positions of the *Planck* clumps and their sizes correspond to the major axis of the clumps reported in the ECC catalog.

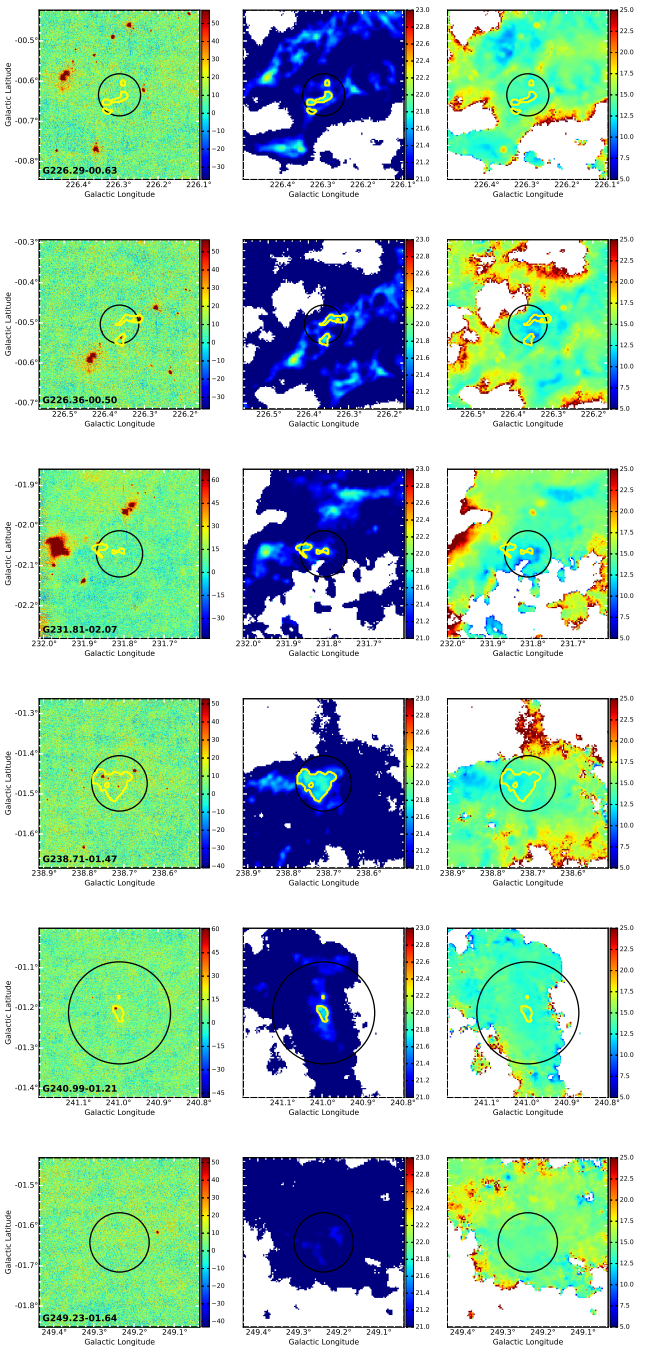


**Fig. D.6.** 70 $\mu$m images ([MJy/sr], *left*) and calculated column density ([cm$^{-2}$], *middle*) in logarithmic scale and dust temperature ([K], *right*) maps with a resolution of 36″. Yellow and red contour levels are at $3 \times 10^{21}$ cm$^{-2}$ and $10^{22}$ cm$^{-2}$, respectively. Black circles are placed at the positions of the *Planck* clumps and their sizes correspond to the major axis of the clumps reported in the ECC catalog.

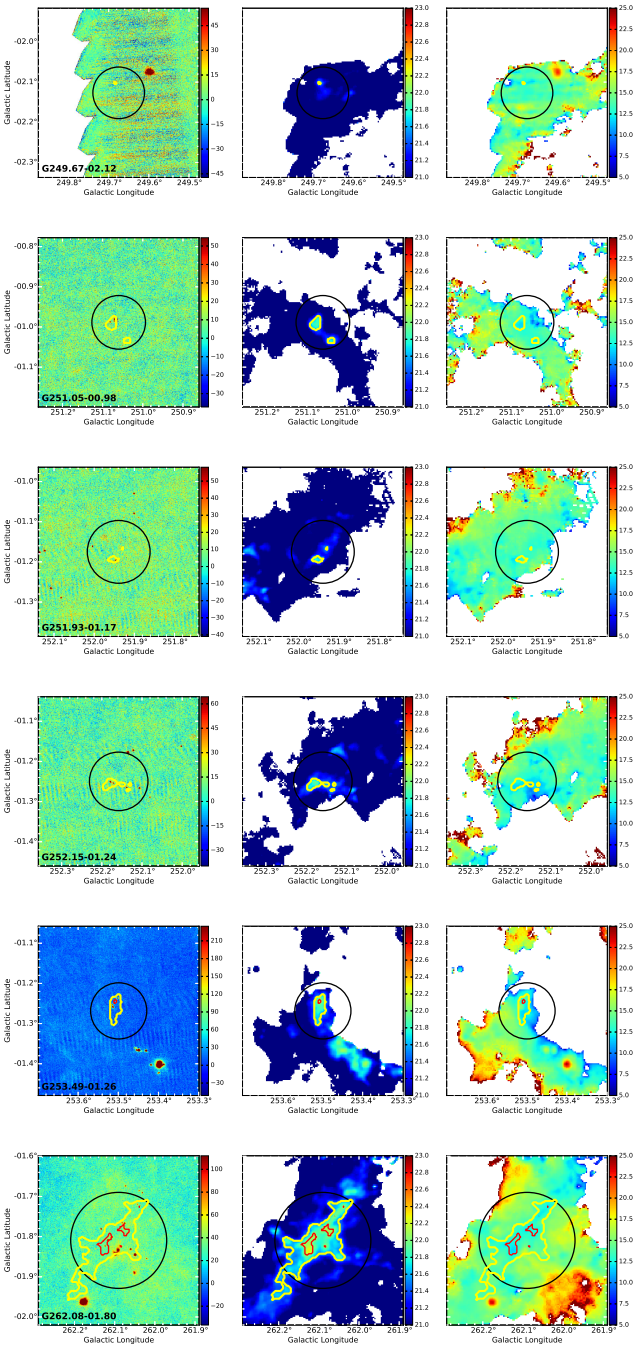


**Fig. D.7.** 70 $\mu$m images ([MJy/sr], *left*) and calculated column density ([cm$^{-2}$], *middle*) in logarithmic scale and dust temperature ([K], *right*) maps with a resolution of 36″. Yellow and red contour levels are at $3 \times 10^{21}$ cm$^{-2}$ and $10^{22}$ cm$^{-2}$, respectively. Black circles are placed at the positions of the *Planck* clumps and their sizes correspond to the major axis of the clumps reported in the ECC catalog.

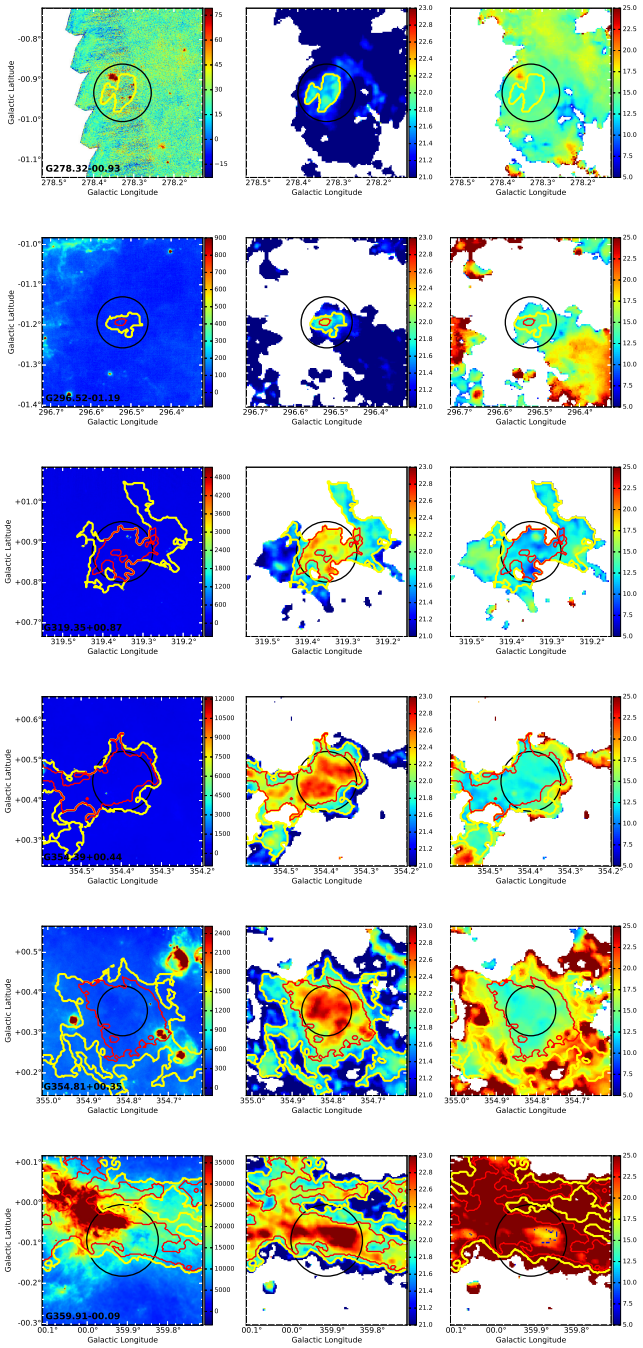


**Fig. D.8.** 70 $\mu$m images ([MJy/sr], *left*) and calculated column density ([cm$^{-2}$], *middle*) in logarithmic scale and dust temperature ([K], *right*) maps with a resolution of 36″. Yellow and red contour levels are at $3 \times 10^{21}$ cm$^{-2}$ and $10^{22}$ cm$^{-2}$, respectively. Black circles are placed at the positions of the *Planck* clumps and their sizes correspond to the major axis of the clumps reported in the ECC catalog.